AFRL-RX-WP-TR-2010-4296

MATERIALS PROCESSING RESEARCH & DEVELOPMENT

Douglas R. Barker, Emmanuel E. Boakye, Michael V. Braginsky, Carmen M. Carney, Yoon Suk Choi, Michael G. Glavicic, Robert L. Goetz, Kristin A. Keller, Young-Won Kim, HeeDong Lee, Pavel Mogilevsky, Triplicane A. Parthasarthy, Satish L. Rao, Oleg N. Senkov, Vikas Sinha, and Youhai Wen

UES, Inc.

AUGUST 2010
Final Report

AIR FORCE RESEARCH LABORATORY
MATERIALS AND MANUFACTURING DIRECTORATE
WRIGHT-PATTERSON AIR FORCE BASE, OH 45433-7750
AIR FORCE MATERIEL COMMAND
UNITED STATES AIR FORCE

NOTICE AND SIGNATURE PAGE

This report was cleared for public release by the USAF 88th Air Base Wing (88 ABW) Public Affairs (PA) Office and is available to the general public, including foreign nationals. Copies may be obtained from the Defense Technical Information Center (DTIC) (http://www.dtic.mil).

AFRL-RX-WP-TR-2010-4296 HAS BEEN REVIEWED AND IS APPROVED FOR PUBLICATION IN ACCORDANCE WITH THE ASSIGNED DISTRIBUTION STATEMENT.

*//Signature//   //Signature//

JOHN H. BARNES, Project Engineer   PAUL L. RET, Chief
Metals Branch   Metals Branch
Metals, Ceramics & NDE Division   Metals, Ceramics & NDE Division
Materials & Manufacturing Directorate   Materials & Manufacturing Directorate

//Signature//

ROBERT T. MARSHALL, Deputy Chief
Metals, Ceramics & NDE Division
Materials & Manufacturing Directorate

This report is published in the interest of scientific and technical information exchange, and its publication does not constitute the Government's approval or disapproval of its ideas or findings.

*Disseminated copies will show "//Signature//" stamped or typed above the signature blocks.

REPORT DOCUMENTATION PAGE

Form Approved
OMB No. 0704-0188

The public reporting burden for this collection of information is estimated to average 1 hour per response, including the time for reviewing instructions, searching existing data sources, gathering and maintaining the data needed, and completing and reviewing the collection of information. Send comments regarding this burden estimate or any other aspect of this collection of information, including suggestions for reducing this burden, to Department of Defense, Washington Headquarters Services, Directorate for Information Operations and Reports (0704-0188), 1215 Jefferson Davis Highway, Suite 1204, Arlington, VA 22202-4302. Respondents should be aware that notwithstanding any other provision of law, no person shall be subject to any penalty for failing to comply with a collection of information if it does not display a currently valid OMB control number. **PLEASE DO NOT RETURN YOUR FORM TO THE ABOVE ADDRESS**.

1. REPORT DATE *(DD-MM-YY)* August 2010	2. REPORT TYPE Final	3. DATES COVERED *(From - To)* 23 November 2004 – 23 August 2010

4. TITLE AND SUBTITLE MATERIALS PROCESSING RESEARCH & DEVELOPMENT	5a. CONTRACT NUMBER FA8650-04-D-5235
	5b. GRANT NUMBER
	5c. PROGRAM ELEMENT NUMBER 62102F

6. AUTHOR(S) Douglas R. Barker, Emmanuel E. Boakye, Michael V. Braginsky, Carmen M. Carney, Yoon Suk Choi, Michael G. Glavicic, Robert L. Goetz, Kristin A. Keller, Young-Won Kim, HeeDong Lee, Pavel Mogilevsky, Triplicane A. Parthasarthy, Satish L. Rao, Oleg N. Senkov, Vikas Sinha, and Youhai Wen	5d. PROJECT NUMBER 2511
	5e. TASK NUMBER 00
	5f. WORK UNIT NUMBER 25110002

7. PERFORMING ORGANIZATION NAME(S) AND ADDRESS(ES) UES, Inc. 4401 Dayton-Xenia Road Dayton, OH 45432-1894	8. PERFORMING ORGANIZATION REPORT NUMBER

9. SPONSORING/MONITORING AGENCY NAME(S) AND ADDRESS(ES) Air Force Research Laboratory Materials and Manufacturing Directorate Wright-Patterson Air Force Base, OH 45433-7750 Air Force Materiel Command United States Air Force	10. SPONSORING/MONITORING AGENCY ACRONYM(S) AFRL/RXL
	11. SPONSORING/MONITORING AGENCY REPORT NUMBER(S) AFRL-RX-WP-TR-2010-4296

12. DISTRIBUTION/AVAILABILITY STATEMENT
Approved for public release; distribution unlimited.

13. SUPPLEMENTARY NOTES
PAO Case Number: 88ABW-2010-4312; Clearance Date: 12 Aug 2010. Report contains color.

14. ABSTRACT

The research reported herein covers the period 23 November 2004 to 23 August 2010. The report covers research on texture, cavitation, and variant selection in titanium alloys, as well as thermomechanical processing of superalloys, in addition to operating a metals processing laboratory that served both internal and external projects. In addition, this report covers research starting in April 2008 on phase field modeling, gamma alloys, bulk metallic glasses, super-high strength cast and wrought aluminum alloy, functional metals, crystal plasticity based FEM modeling, and mesoscale dislocation evolution modeling. Much of this research has been published elsewhere in the open literature as journal articles and papers.

15. SUBJECT TERMS
metals, nickel alloys, titanium alloys, beta gamma alloys, plasticity, metallic glasses, ceramic composites, TPS, UHTCs

16. SECURITY CLASSIFICATION OF:			17. LIMITATION OF ABSTRACT: SAR	18. NUMBER OF PAGES 56	19a. NAME OF RESPONSIBLE PERSON (Monitor) John H. Barnes
a. REPORT Unclassified	b. ABSTRACT Unclassified	c. THIS PAGE Unclassified			19b. TELEPHONE NUMBER *(Include Area Code)* N/A

Standard Form 298 (Rev. 8-98)
Prescribed by ANSI Std. Z39-18

Table of Contents

List of Figures

List of Tables

FOREWORD

This report was prepared by the Materials and Processes Division of UES, Inc., Dayton, Ohio under Air Force Contract No. FA8650-04-D-5235. Mr. John H. Barnes of the Metals, Ceramics and Non-Destructive Evaluation Division of the Air Force Research Laboratory (AFRL) was the Government Project Engineer. The research reported herein covers the period 23 November 2004 to 23 August 2010. The report covers research conducted during this period on texture, cavitation, and variant selection in titanium alloys, as well as thermomechanical processing of superalloys, in addition to maintaining a fully operational metals processing high bay that served both internal and external projects. In addition, this report covers research starting in April 2008 on phase field modeling, gamma alloys, bulk metallic glasses, super-high strength cast and wrought aluminum alloy, functional metals, crystal plasticity based FEM modeling, and mesoscale dislocation evolution modeling.

1 Executive Summary

The objectives of this program were to (1) investigate and determine the processing conditions required to achieve desired microstructures and mechanical properties in advanced aerospace materials, (2) implement and use analytical models for process design in the Materials Processing Laboratory (MPL), (3) validate analytical models by physical modeling, and (4) create a center of excellence for materials processing. Primary emphasis was given to composites and high temperature materials used in advanced engines and structures.

Materials of various types and compositions were studied. In several cases, a full-fledged processing science approach was utilized, in which the material was fully characterized in terms of microstructure and flow behavior, the proposed processing method was modeled analytically, the actual processing was carried out in the MPL and the analytical model was validated with experimental measurements. In other cases, some of these steps were eliminated when the material or process was well understood.

Starting in April 2008, additional research goals were undertaken under government directive. The objectives were broadened to include (4) phase field modeling of nickel base alloys towards predictions of microstructural evolution, (5) development of Gamma and Beta-Gamma titanium alloys towards rolled sheets for thermal protection applications, (6) exploration of bulk metallic glasses as engineering alloys, (7) development of a super-high strength aluminum alloy for use in cast form for rocket engine pump housing and in wrought form for turbines, (8) development of crystal plasticity based finite element method (FEM) to model and understand polycrystal deformation, and (9) discrete dislocation simulations in three-dimensional volumes of metals.

The research studies resulted in many interesting and technologically useful findings, which were published in recognized journals, after obtaining clearance for public release from the appropriate approving authority.

This report describes the outcomes of the research in the following format. First, Published Research has been divided into sections based on above-mentioned objectives. In each section, an abstract of each successful outcome is presented along with a reference to the publications (listed at the very end of the document under References) where more details can be found. Second, work not yet published or not cleared for public release, is presented under Unpublished Research. This section is followed by a listing of all publications, presentations and reports resulting from this funding source.

2 Published Research

2.1 Published Research on Texture of Ti-6Al-4V

2.1.1 A Method to Measure the Texture of Secondary Alpha in Bimodal Titanium-Alloy Microstructures

A general method for determining the texture of the secondary-alpha phase in titanium alloys with a bimodal microstructure was developed. Validated using Ti-6Al-4V, the procedure is generally applicable to all alpha-beta titanium alloys and can be applied using a variety of texture-measurement techniques. This work was published in *Script Materialia* by Glavicic, Miller, and Semiatin [1].

2.1.2 Modeling of Texture Evolution during Hot Forging of Alpha/Beta Titanium Alloys

Texture development during the subtransus hot forging of alpha/beta titanium alloys with an equiaxed-alpha microstructure was modeled using the Los Alamos polycrystalline plasticity (LApp) code and ah111ipencil-glide polycrystalline plasticity code coupled with the FEM program DEFORM™. The methodology treated the partitioning of the imposed strain between the alpha and beta phases, and thus enabled the prediction of the distinct deformation textures developed in the primary alpha and beta matrix during hot working. Two variant selection rules in conjunction with the beta deformation texture were also examined to establish a method for predicting the transformation texture of secondary alpha developed as a result of beta decomposition during cooldown following forging or heat treatment. The approach was validated via an industrial-scale trial comprising hot pancake forging of Ti-6Al-4V. This work was published in *Metallurgical and Materials Transactions A* by Glavicic, Goetz, Barker, Shen, Furrer, Woodfield, and Semiatin [2].

2.1.3 Modeling and Simulation of Texture Evolution during the Thermomechanical Processing of Titanium Alloys

The development of crystallographic texture, the preferred orientation of grains in a polycrystalline aggregate, during thermomechanical processing can play an important role with regard to the secondary forming response (e.g., deep drawing of sheet) and service performance (e.g., strength, elastic modulus, ductility, fracture toughness) of metallic materials. Crystallographic texture, or simply texture for succinctness, may arise as a result of large-strain deformation, dynamic/static recrystallization, grain growth, or phase transformation. A second form of anisotropy, mechanical texturing or mechanical fibering, refers to the alignment of microstructure, inclusions, and so forth during deformation processes and may also affect mechanical properties such as ductility and fracture toughness. This latter form of texture is not discussed in the present article. This work was published in *ASM Handbook 22A: Fundamentals of Modeling for Metals Processing* by Semiatin, Glavicic, Shevchenko, and Ivasishin [3].

2.1.4 The Origins of Microstexture in Duplex Ti Alloys

A previously developed methodology was used to transform electron backscatter diffraction (EBSD) data for the primary and secondary alpha phases of Ti-6Al-2Sn4Zr-6Mo (Ti-6246) to

the prior beta phase. The results established that the observed microtexture in duplex alloys is a direct result of the prior beta grain orientations, and variant selection. In addition, for a homogeneous duplex microstructure, all of the secondary alpha phase and the majority of the primary alpha grains retain crystallographic coherency, according to the Burgers relationship, with the surrounding beta phase matrix, which comprise prior beta grains. This investigation establishes that this technique to recover the prior beta grain orientations is applicable to duplex α/β titanium microstructures. The crystallographic coherency of the primary and secondary alpha phase with the prior beta grain coupled with variant selection then leads to the localized microtexture observed in a wide variety of Ti alloys. This work was published in *Materials Science and Engineering A* by Glavicic, Bartha, Jha, and Szczepanski [4].

2.1.5   X-Ray Line Broadening Investigation of Deformation during Hot Rolling of Ti-6Al-4V with a Colony-Alpha Microstructure

X-ray line-broadening techniques that were previously developed and applied to quantify deformation behavior during the hot rolling of commercial-purity titanium were applied to Ti–6Al–4V plate with a colony-alpha preform microstructure. The work quantified the challenges in using line-broadening techniques for two-phase titanium alloys which undergo a phase transformation during cooling following hot working. This work was published in *Acta Materialia* by Glavicic and Semiatin [5].

2.2   Published Research on Cavitation of Ti-6Al-4V

2.2.1   Cavitation during Hot-Torsion Testing of Ti-6Al-4V

Hot-torsion testing was used to establish the cavitation behavior of a typical alpha/beta titanium alloy, Ti-6Al-4V, with a colony microstructure, during simple-shear deformation. For this purpose, sections of deformed specimens were examined by optical metallography, and by scanning and orientation imaging microscopy (OIM). It was found that cavity nucleation occurred along prior beta boundaries as well as at triple points; in particular, most cavities nucleated along boundaries perpendicular to the axial direction of the specimen. Extensive growth was observed for cavities surrounded by both hard and soft orientations, with the soft colonies accommodating more of the imposed strain. At high degrees of deformation, dynamic globularization of the colony microstructure adjacent to the cavities was also observed. In addition, the metallographic observations revealed that the cavities did not grow in an equiaxed mode, but in an elliptical manner. A tensor describing the cavity-growth rate along the axial, radial, and hoop specimen directions was determined using measurements of individual cavity sizes. The cavity-growth behavior in torsion was compared to previous observations from hot-tension tests. This comparison indicated that the rate of cavity growth in shear was approximately one-tenth that in uniaxial tension. This finding is in broad agreement with models predicting the variation of the cavity-growth rate as a function of the ratio of the mean stress to the hydrostatic stress. This work was published in *Metallurgical and Materials Transactions A* by Nicolaou, Miller, and Semiatin [6].

2.2.2 The Effect of Strain-Path Reversal on Cavitation during Hot Torsion of Ti-6Al-4V

The effect of strain-path reversal on cavitation behavior during the hot torsion testing of an alpha/beta titanium alloy, Ti-6Al-4V, with a colony-alpha microstructure was established. Optical microscopy was used to measure cavitation parameters such as cavity size, density, and area fraction. It was observed that when the torsion direction is reversed, the cavitation process is reversed as well; i.e., cavity shrinkage takes place. The experimental observations were interpreted in the context of previous models developed for the densification of porous bodies. For this purpose, the models were modified to treat the effect of colony orientation on the local stress state and the accommodation of the externally imposed strain, both of which affect the rate of densification/cavity shrinkage. A modified version of the AFRL PM-consolidation model was shown to provide reasonable estimates of the shrinkage kinetics. An alternate description of cavity shrinkage during reversed torsion, analogous to prior descriptions of cavity growth, was also developed. It was concluded that the absolute magnitude of the cavity shrinkage rate is smaller than its counterpart during growth because the local stress ratio is lower during reversed straining compared to that during forward straining. This work was published in *Metallurgical and Materials Transactions A* by Nicolaou and Semiatin [7].

2.2.3 Effect of Strain-Path Reveral on Microstructure Evolution and Cavitation during Hot Torsion Testing of Ti-6Al-4V

Hot torsion testing comprising multiple twist reversals was used to establish the effect of strainpath changes on concurrent dynamic globularization and cavitation of Ti-6Al-4V with a colony-alpha starting microstructure. Optical microscopy was used to quantify the cavity area fraction and the effect of globularization on cavitation. The deformation of the hard and soft colonies surrounding the largest cavities and self-consistent-model calculations of strain partitioning were used to estimate the macroscopic and local strains at which colonies with different strengths globularize. It was found that both hard and soft colonies undergo dynamic globularization at the same local strain (i.e., strain within the colony). In addition, cavitation behavior during torsion with multiple strain-path changes was interpreted by taking into account the breakup of the colonies into a globular structure. It was found that cavity growth (or shrinkage) persisted as long as there was a flow-stress difference in adjacent regions/colonies surrounding a given cavity. When the microstructure became uniform (as in the case of full globularization), the cavity area fraction did not measurably change with subsequent additional deformation. This work was submitted for publication in *Metallurgical and Materials Transactions A* by Nicolaou and Semiatin [8].

2.2.4 Effect of Stress and Strain Path on Cavity Closure during Hot Working of an Alpha/Beta Titanium Alloy

The effect of strain path and stress state on deformation and cavitation during hot working of Ti-6Al-4V was established via torsion-compression and reversed-torsion tests. Measurements of the cavity area fraction and the size of individual cavities revealed that the rate of cavity closure during the change in strain path following torsion is approximately twice as large in compression compared to reversed torsion. The observations were interpreted in the context of the effect of texture on local stress state and a micromechanical model for the consolidation of porous media. From an engineering standpoint, this work also indicated that the rate of cavity closure decreases

with increasing deformation, thus suggesting that very large strains may be required to totally heal damage. This work was published in *Metallurgical and Materials Transactions A* by Nicolaou, Goetz, and Semiatin [9].

2.2.5   Effect of Deformation and Prestrain Mode on the Flow Behavior of Ti-6Al-4V

The effect of strain path on the plastic-flow behavior of Ti-6Al-4V with a colony-alpha perform microstructure was determined. Specifically, the stress-strain response in compression following a prestrain via torsion, compression, or rolling was interpreted. It was found that the flow-softening parameter was dependent on the level of the prestrain, but independent of the mode of prestrain. After a prestrain of 0.3, however, it decreased very slowly. This work was submitted for publication to *Metallurgical and Materials Transactions A* by Nicolaou and Semiatin [10].

2.2.6   Dynamic-Coarsening Behavior of an α/β Titanium Alloy

The dynamic-coarsening behavior of Ti-6Al-4V with an equiaxed α microstructure was established via isothermal hot-compression testing of cylindrical samples cut from an ultra-fine-grain-size (UFG) billet. Compression experiments were conducted at 900 and 955 °C, strain rates between 10^{-4} and 1 s^{-1}, and imposed true strains between 0 and 1.4. Following deformation, quantitative metallography revealed marked coarsening of the primary α particles at low strain rates (10^{-4} and 10^{-3} s^{-1}). The dynamic coarsening rate followed r^n vs. time kinetics, in which n was between 2 and 3, or behavior between those of bulk-diffusion and interface-reaction controlled. An examination of the temperature and strain-rate dependence of theoretical coarsening rates, however, strongly suggested that bulk diffusion (with $n = 3$) was more important. The dynamic-coarsening behavior was also interpreted in the context of the observed plastic-flow behavior. At low strain rates, high values of the strain-rate sensitivity ($m = 0.5$) and the overall shape of log stress–log strain rate plots indicated that the majority of the imposed strain was accommodated by grain-boundary sliding (gbs) and only a small amount via dislocation glide/climb processes. In addition, an analysis of the flow hardening that accompanied dynamic coarsening indicated that the flow stress varied approximately linearly with the α particle size, thus providing support for models based on gbs accommodation by dislocation activity in grain-mantle regions. This work was published in *Metallurgical and Materials Transactions A* by Semiatin, Corbett, Fagin, Salishchev, and Lee [11].

2.3   Published Research on Variant Selection of Ti-6Al-4V

2.3.1   Low-Temperature Coarsening and Plastic Flow Behavior of an Alpha/Beta Titanium Billet Material with an Ultrafine Microstructure

The influence of microstructure evolution on the low-temperature superplasticity of ultrafine alpha/beta titanium alloys was established. For this purpose, the static and dynamic coarsening response and plastic flow behavior of Ti-6Al-4V with a submicrocrystalline microstructure were determined via a series of heat treatments and uniaxial compression tests at temperatures of 650 °C, 775 °C, and 815 °C. At all test temperatures, static coarsening exhibited diffusion controlled (r^3 *vs.* time) kinetics and followed a dependence on phase composition and volume fraction qualitatively similar to previous observations at 850 °C to 950 °C. Dynamic coarsening at 775 °C and 815 °C and strain rates of 10^{-4} and 10^{-3} s^{-1} were similar to prior higher temperature

observations as well in that the kinetics were approximately one order of magnitude faster than the corresponding static behaviors. The increase in coarsening rate with superimposed deformation was attributed to the enhancement of diffusion by dislocations generated in the softer beta phase. With respect to deformation response, plastic flow was superplastic with m values of ~0.6 at 650 °C, 775 °C, and 815 °C and strain rates of 10^{-4} and 10^{-3} s^{-1}. Dynamic coarsening resulted in flow hardening at both temperatures and strain rates for a short preheat time (15 minutes) but was noticeably reduced when a longer preheat time (one hour) was used prior to testing at 10^{-3} s^{-1}. The latter behavior was largely attributed to noticeable static coarsening during preheating. A generalized constitutive relation based on a single stress exponent and the instantaneous alpha particle size was shown to describe the superplastic flow of ultrafine Ti-6Al-4V at low and high temperatures. This work was published in *Metallurgical and Materials Transactions A* by Sargent, Zane, Fagin, Ghosh, and Semiatin [12].

2.3.2 Plastic Flow and Microstructure Evolution during Low-Temperature Superplasticity of Ultrafine Ti-6Al-4V Sheet Material

The low-temperature superplastic (SP) flow behavior of two lots of Ti-6Al-4V sheet, each with an ultrafine microstructure, was established by performing tension tests at temperatures of 775 °C and 815 °C and true strain rates of 10^{-4} and 10^{-3} s^{-1}. The as-received microstructures of the two materials comprised either equiaxed or slightly elongated alpha particles in a beta matrix. The material with equiaxed alpha particles exhibited flow hardening, which was correlated with concurrent (dynamic) coarsening. The rate of dynamic coarsening was rationalized in terms of static coarsening measurements and the enhancement of kinetics due to pipe diffusion. By contrast, the material with initially elongated alpha particles exhibited comparable flow hardening at the lower strain rate but a complex, near-steady-state behavior at the higher strain rate. These latter observations were explained on the basis of the evolution of the alpha particle shape and size during straining; dynamic coarsening or dynamic spheroidization was concluded to be most important at the lower and higher strain rates, respectively. The plastic flow behavior was interpreted in the context of a long-wavelength flow localization analysis. This work was published in *Metallurgical and Materials Transactions A* by Semiatin, Fagin, Betten, Zane, Ghosh, and Sargent [13].

2.3.3 Constitutive Modeling of Low-Temperature Superplastic Flow of Ultrafine Ti-6Al-4V Sheet Material

The low-temperature superplastic flow behavior of two lots of Ti-6Al-4V sheet with an ultrafine microstructure was modeled. One lot (Sheet A) had an equiaxed-alpha starting microstructure; the flow stress/flow hardening exhibited by this material was explained on the basis of the Bird-Mukherjee-Dorn constitutive equation. The other material (Sheet B), having a mixed equiaxed- and remnant-lamellar alpha microstructure, underwent flow softening, flow hardening, or steady-state flow depending on test temperature and strain rate. These behaviors were interpreted in the context of a dynamic spheroidization model. The apparent flow softening at the end of all of the flow curves was explained using a simple flow-localization model. This work was published in *Key Engineering Materials Journal* by *Trans Tech Publications* by Semiatin and Sargent [14].

2.4   Published Research on Superalloys

2.4.1   Deformation and Recrystallization during Thermomechanical Processing of a Nickel-Base Superalloy Ingot Material

The deformation response and recrystallization behavior of a coarse, columnar-grain superalloy ingot material, Waspaloy, with a <100> fiber texture were established. For this purpose, isothermal hot compression tests were performed on cylindrical and double-cone samples at supersolvus temperatures under both monotonic (constant strain rate) and multi-hit conditions. Plastic flow showed a noticeable dependence on test direction relative to the columnar-grain orientation; the observed anisotropy in peak flow stress and flow softening were explained on the basis of the evolution of crystallographic texture during recrystallization. Similarly, anisotropy in dynamic recrystallization kinetics with respect to test direction was interpreted in terms of the effect of initial texture on the plastic work imposed per increment of macroscopic strain. Nevertheless, the broad kinetics for the coarse-grain, ingot material deformed under both monotonic and multi-hit conditions were comparable to those previously measured for *fine-grain*, wrought Waspaloy. Such an effect was attributed to the beneficial influence of the nucleation of recrystallization at both grain boundaries and carbide particles in the ingot material. In addition, a spatial non-uniformity in recrystallization was found in the ingot material and was interpreted in the context of the grain-boundary character and non-uniform strain at the grain/intragrain scale. A suite of tools being developed to model recrystallization phenomena during the breakdown of superalloy ingots is described. These tools include a mechanistic cellular automata; a mesoscale, mechanism-based model; and the crystal-plasticity finite-element method. This work was published in *Material Science Form* by Semiatin, Weaver, Goetz, Thomas, and Turner [15].

2.4.2   Defect Occurrence and Modeling forthe Thermomechanical Processing of Aerospace Alloys

Mechanism-based models for the evolution of defects during the thermomechanical processing of aerospace titanium- and nickel-based alloys are reviewed. These defects include those comprising microstructural/metal-flow irregularities and those that are damage related (i.e., cracks and cavities). The development of undesirable/nonuniform microstructures and cavities during the mill processing of alpha/beta titanium alloys is addressed first. Relatively simple, diffusion-based models of spheroidization and coarsening are applied to quantify the propensity for microstructure nonuniformities. Similarly, first-order micromechanical models have been formulated to estimate the effect of local crystallographic texture on nonuniform flow, the generation of triaxial stresses, and cavity growth/closure in alpha/beta titanium alloys with a colony-alpha microstructure. The occurrence of nonuniform grain structures (and so-called ALA, or "as large as," grains) in cast, wrought, and powder-metallurgy superalloys is also discussed. A physics-based model to treat the topology of recrystallization and the evolution of ALA grains in such materials is proposed. This work was published in *Journal of Engineering Materials and Technology* by Semiatin, Nicolaou, Thomas and Turner [16].

2.5   Published Research on Phase Modeling

2.5.1   A Ternary Phase-Field Model Incorporating Commercial CALPHAD Software

A ternary phase-field model was developed that is linked directly to commercial CALPHAD software to provide quantitative thermodynamic driving forces. A recently available diffusion mobility database for ordered phases is also implemented to give a better description of the diffusion behavior in alloys. Because the targeted application of this model is the study of precipitation in Ni-based superalloys, a Ni-Al-Cr model alloy was constructed. A detailed description of this model is given in the paper. We have considered the misfit effects of the two solute elements. Transformation rules of the dual representation of the Ɣ + Ɣ′ microstructure by CALPHAD and by the Phase-Field are established and the link with commercial CALPHAD software id described. Proof-of-concept tests were performed to evaluate the model and the results demonstrate that the model can accurately describe the compositional and structural changes associated with precipitation of the Ɣ′ phase. Uphill diffusion of Al is observed in a few diffusion couples showing the significant influence of Cr on the chemical potential of Al. Possible applications of this model are discussed. This work was published in *Acta Materialia* by Wen, Lill, Chen, and Simmons [17].

2.5.2   Local Interface Effects on Coalescence Kinetics in Ni-Base Alloys

Coalescence of precipitates is a common kinetic phenomenon. The phase-field method can simulate coalescence of precipitates without any ad hoc assumptions. However, independent of long range effects (e.g. lattic misfit) the method predicts a high coalescence rate when applied to systems with a high volume fraction of precipitates. We show that this is a result of ignoring the local phenomenon in the interface regions, which is an approximation adopted by many other simulation techniques. An improved coalescence rate is achieved by property addressing this local phenomenon through introducing composition and phase dependence of diffusion mobility. This work was published in *Modelling and Simulation in Materials Science and Engineering* by Wen, Simmons, and Woodward [18].

2.5.3   Systematic Approach to Microstructure Design of Ni-Base Alloys Using Classical Nucleation and Growth Relations Coupled with Phase Field Modeling

To analyze the formation of bimodal particle size distributions during precipitation, the dynamic competition for supersaturation by growth of existing precipitates and nucleation of new particles was studied under continuous cooling conditions with constant cooling rates. The nucleation rate was calculated according to classical nucleation theory as a function of local supersaturation and temperature. The depletion of matrix supersaturation by growth of existing particles was calculated from fully diffusion-controlled precipate growth in an infinite matrix. Phase field simulations of Ɣ′ precipitation in a binary Ni-Al alloy were preformed under continuous cooling conditions. Then the average and maximum matrix supersaturations were calculated and plotted onto the contours of nucleation rate and growth rate in concentration and temperature space. These methods were used iteratively to identify the window for bimodal particle size distributions. This work was published in *Metallurgical and Materials Transactions A* by B. Wang, Y.H. Wen, J.P. Simmons, and Y. Wang [19].

2.6 Published Research on Gamma Alloy

2.6.1 Microstructure Changes and Estimated Strengthening Contributions in a Gamma Alloy Ti-45Al-5Bn Pack-Rolled Sheet

Thin sheets made of a gamma-titanium aluminide alloy, Ti-45Al-5Nb, produced by a patented pack-rolling process, were evaluated for microstructure variation and evolution taking place during aging and annealing treatments. The as-received sheet material was characterized by remarkably high yield strength, 810MPa, and a complex bimodal microstructure. The microstructure consisted of a matrix of twinned gamma-phase grains and fine-lath lamellar-grain microconstituent, together with a dispersed ultra-fine-grained gamma + alpha-2 mixture microconstituent. High-temperature isothermal aging treatments changed the microstructure to a stable mixture of gamma-phase grains (matrix) and coarse alpha-2 phase particles, having size distributions and volume fractions that were specific to the aging temperature. A concurrent strength loss reflects this trend and results in a stable strength level of 550 MPa upon aging at 1000 °C for 144h. Using composition estimates from the phase-boundary shifts that occur from the Nb addition to a Ti-45Al base alloy and, the rule of mixtures, an analysis was made to show that the gamma- phase matrix has an intrinsic strength of 178MPa. This is a significant intrinsic strength level, well over that of ~70MPa for the Ti-45Al binary alloy. This is rationalized as the solid-solution strengthening effect from shifts of the Ti and Nb levels in the gamma phase and, by an added effect due to increased oxygen solubility in the gamma phase. The overall strength of Ti-45Al-5Nb, however, is roughly the same as that of Ti-45Al, and this is explained by a drastic reduction in the volume fraction of alpha-2 phase in Ti-45Al-5Nb alloy, which is a result of the Nb-induced phase-boundary shifts. This work was submitted was published in *Intermetallics* by Kim, Rosenberger and Dimiduk [20].

2.6.2 Metallic Thermal Protection System Materials: Beta Gamma Sheet Alloy/Process Development

The Air Force of the future will require revolutionary capabilities in space access and hypersonic flight. Achieving these high velocity flight capabilities will require systems with the ability to survive the very high temperature environment created by high supersonic and hypersonic flight. To protect the vehicles from the extreme temperature environment, thermal protection systems (TPS) and hot structures will be used. A spectrum of materials that maintain properties at high temperatures will be required. The systems will span the spectrum from expendable missile systems to reusable access to space; from scramjet propulsion to hot aero-structures. Reusable systems will require aircraft-like vehicle operations and maintenance support to allow the next generation of vehicles to economically support future USAF missions. Responsive, reliable, near all-weather operations is a must and turnaround times need to be in days to hours, not weeks. Performance of hypersonic weapon systems, responsive access to space, scramjet propulsion, etc. will be enhanced through the incorporation of innovative, low density TPS concepts. Gamma titanium aluminide alloys (gamma alloys) possess the attractive combination of low density (~50 percent of that of superalloys) and high temperature (up to 1500 °F or 815 °C) capability that are ideal for hot airframe structure and propulsion applications. Yet, gamma alloys have not been inserted into aerospace service due to their material and manufacturing limitations. One of the limitations is low ductility at room temperature resulting in design difficulties and lower damage tolerance. A new class of TiAl-based alloys, called beta gamma,

were evaluated to determine if they would reduce the limitations. Unlike existing gamma alloys, beta gamma alloys are designed such that the ductile β phase volume fraction is adequate to enhance processing and increase the room temperature ductility while maintaining adequate performance at the use temperature. The alloys also feature significant grain refinement and compositional homogeneity. Utilizing such beneficial beta-phase distribution and microstructure features, demonstration has been made to develop the alloy/process technology to produce low-cost beta gamma alloy mill products such as thin sheets and rectangular bars with potentially improved properties. These low-density (~4.1g/cm^3) products showed application potential to be used at high temperatures at least up to 1500 °F (815 °C) for airframe and propulsion structures. This work is in the process of being submitted to AFRL-RX as a Technical Report by Young-Won Kim [21].

2.7 Published Research on Mechanical Properties of Bulk Metallic Gasses

2.7.1 Observation of Shear Thickening during Compressive Flow of $Mg_{54}Y_{11}Ag_7Cu_{28}$ in the Supercooked Liquid Range

Uniaxial compression tests of $Mg_{54}Y_{11}Ag_7Cu_{28}$ metallic glass were performed in the supercooled liquid region (468 K) at a strain rate range of 5×10^{-4} to 2×10^{-3} s^{-1}. In the course of testing, shear thickening behavior was observed, where the magnitude of the peak stress increases with increasing initial strain rate. The deformation behavior of the glassy metal is discussed with emphasis on the commonly reported stress overshoot, strain softening behavior, and the previously unreported shear thickening behavior observed. This work was published in *Metallurgical and Materials Transactions A* by Ross, Mishra, Senkov, and Miracle [22].

2.7.2 Mechanical and Fatigue Behavior of $Ca_{65}Mg_{15}Zn_{20}$ Bulk-Metallic Glass

A number of Bulk Metallic Glasses (BMGs), such as Zr-, Fe-, Pd-, Al-, and Ni-based alloys, have been discovered after the rapid development of glass-forming alloys during the early 1990s. Ca-Mg-Cu and Ca-Mg-Cu-Ag BMGs were successfully fabricated by Amiya and Inoue in 2002. Following these reports, numerous Ca-based BMG systems have been produced and studied. Ca-based BMG alloys are of interest because of their unique properties, such as low density (~2.0g cc^{-1}), low Young's modulus (~17 GPa to 20 GPa) that is comparable to the modulus of human bones, low glass-transition temperature (T_g ~100 °C) and a wide super-cooled liquid temperature range ($\Delta T_{xg} = T_x - T_g$ ~30 to 808 °C). Elements such as Ca, Mg, and Zn are biocompatible, which makes the Ca-Mg-Zn-based alloys attractive for use in biomedical applications. The amorphous structure gives unique properties to BMGs, including high elastic strain, high fracture strength, and high fatigue resistance. Although the mechanical behavior of BMGs is studied widely, there is no fatigue data for Ca-based BMGs. A comprehensive understanding based on the compression, hardness, and fatigue behavior is critically important for the application of the Ca-based BMGs. In the current paper, the compression behavior, Vickers hardness, and fatigue characteristics of $Ca_{65}Mg_{15}Zn_{20}$ BMGs were investigated at room temperature in air. A mechanistic understanding of the fatigue and fracture mechanisms of Ca-based BMGs is proposed. This work was published in *Advanced Engineering Materials* by Wang, Liaw, Senkov, Miracle, and Morrison [23].

2.7.3 Fatigue and Fracture Behavior of a Ca-Based Bulk–Metallic Glass

The compression and fatigue behavior of a $Ca_{65}Mg_{15}Zn_{20}$ bulk-metallic glass was studied in air at room temperature. During the preparation of cubical samples of the $Ca_{65}Mg_{15}Zn_{20}$ for compression and fatigue investigations, small spherical cavities were found. Under both monotonic and cyclic compression loadings of the samples, fractures initiated at these cavities and propagated in a direction generally parallel to the loading axis. Finite-element analysis was used to model the fracture behavior. The FEA of a centrally located spherical void showed that under compression loading, large tensile stresses evolved in the cavities. The orientation of the maximum principal stress (P1) was found to be normal to the direction of crack propagation, which is consistent with the experimental finding. Stresses in deeply embedded adjacent voids and those in superficial voids were also studied. The influence of the void location in the cubical sample on the fracture behavior was quantitatively discussed. This work was published in *Metallurgical and Materials Transactions A* by Raphael, Wang, Liaw, Senkov, and Miracle [24].

2.8 Published Research on Thermodynamic and Kinetic Behavior of Supercooled Glass-Forming Liquids

2.8.1 Description of the Fragile Behavior of Glass Forming Liquids with the Use of Experimentally Accessible Parameters

The three-fitting-parameter viscosity equations, i.e. Vogel-Fulcher-Tamman (VFT) and Avramov's equations, which are used to describe the temperature dependence of viscosity are modified into one-fitting parameter equations. Both modified equations contain the glass transition temperature Tg and fragility index m as material constants, allowing a direct comparison of the modified equations. Based on analysis of 12 glass-forming liquids, it is concluded that the modified Avramov's equation describes the experimental data slightly better than the modified VFT equation. Experimental data must be collected over a wide temperature range before the three fitting parameters of the VFT and Avramov equations can be determined and the equations can be applied. However, the modified equations developed here provide a convenient method of estimating the temperature dependence of viscosity by using the experimentally accessible parameters Tg and m, which can be determined by differential scanning calorimetry measurements conducted in a narrow temperature range near the glass transition temperature. This work was published in the *Journal of Non-Crystalline Solids* by Senkov and Miracle [25].

2.8.2 Relaxation Behavior of Ca-Based Bulk Metallic Glasses

Relaxation behavior of $Ca_{60}Mg_{20}Zn_{20}$, $Ca_{60}Mg_{20}Cu_{20}$, $Ca_{65}Mg_{15}Zn_{20}$, $Ca_{50}Mg_{20}Cu_{30}$, and $Ca_{55}Mg_{18}Zn_{11}Cu_{16}$ bulk metallic glasses was determined in the glass transition region using differential scanning calorimetry (DSC) with the heating rates from 1 K/min to 160 K/min. The activation enthalpy of structural relaxation and the fragility index m were found to be smaller in the glassy state (onset of the glass transition) than in the supercooled liquid state (end of glass transition). The Ca-based glass-forming liquids showed strong behavior of the relaxation time, with the fragility indexes m in the range of 33 to 40. The strong liquid behavior implies sluggish kinetics of crystallization in the supercooled liquid region and explain the very good glass forming ability of these alloys. The critical cooling rate for amorphization R_c of the Ca-based

bulk metallic glasses was estimated to be in the range of 0.3 to 10 K/s, which is similar to R_c values for the best Pd and Zr based metallic glass forming alloys discovered so far. This work was submitted for publication to *Metallurgical and Materials Transactions A* by Senkov and Miracle [26].

2.9   Published Reseach on a Nanocrystallin Aluminum Alloy from Amorphous Powder

2.9.1   Consolidation of Amorphous Aluminum Alloy Powder by Equal Channel Angular Extrusion

Semi-amorphous aluminum alloy powders produced by gas atomization were compacted using equal channel angular extrusion (ECAE) in the temperature range of 200 °C to 300 ºC. Microstructures of the compacts were studied after different levels of ECAE deformation, which allowed analysis of the mechanism of particle interactions, deformation and bonding during different stages of consolidation. Very non-homogeneous deformation of the compacted material was detected. At the temperatures of compaction, amorphous powder particles were much softer than fully crystalline powder particles, and they were severely deformed while the crystalline particles remained nearly spherical. Almost full consolidation occurred in regions predominantly consisting of amorphous and semi-amorphous powder particles at true strains of ~2. However, further excessive deformation led to strain localization and shear crack formation in the consolidated regions. Regions dominated by fully crystalline spherical particles with brittle intermetallic phases showed poor consolidation due to particle rotations and particle fracture; leading to weak particle bonding. The results show that consolidation is impeded by the presence of fully crystalline particles in the powder. This work was published in *Materials Science Forum* by Senkov [27].

2.10   Published Research on Super-High Strength Cast-and-Wrought Aluminum Alloys

2.10.1 Precipitation of Al$_3$(Sc,Zr) Particles in a Direct Chill Cash Al-Zn-Mg-Cu-Sc-Zr Alloy during Conventional Solution Heat Treatment and its Effect on Tensile Properies

The chemical partitioning of alloying elements between the disordered y and ordered y' phases in the nickel base superalloy Rene 88DT, has been characterized in detail using three dimensional atom probe tomography coupled with energy-filtered transmission electron microscopy studies. After a homogenization treatment followed by a water quench, it is observed that the morphology of the y' precipitates remains near-spherical even after long aging times. Compositional variation, observed between small (<5 nm) and larger y' precipitates, reduces with increasing aging time, while the compositional gradient across the y/y' interface decreases. The process of growth of y' precipitates seems to occur through coalescence of adjacent y' precipitates, facilitated through the formation of "necks" between adjacent precipitates. These necks are observed to have intermediate elemental concentration values, between the matrix and the y' precipitate compositions. The chemical partitioning of alloying elements between the disordered y and ordered y' phases in the nickel base superalloy Rene 88DT, has been characterized in detail using three dimensional atom probe tomography coupled with energy-filtered transmission electron microscopy studies. After a homogenization treatment followed by a water quench, it is observed that the morphology of the y' precipitates remains near-spherical even after long aging times. Compositional variation, observed between small (<5 nm) and larger

12

y' precipitates, reduces with increasing aging time, while the compositional gradient across the y/y' interface decreases. The process of growth of y' precipitates seems to occur through coalescence of adjacent y' precipitates, facilitated through the formation of "necks" between adjacent precipitates. These necks are observed to have intermediate elemental concentration values, between the matrix and the y' precipitate compositions. This work was published in *Acta Materialia* by Senkov, Shagiev, Senkova, and Miracle [28].

2.10.2 Effect of Al$_3$ (Sc,Zr) Particles on Tensile Properties of An Al-Zn-Mg-Cu-Sc-Zr Alloy

Small additions of Sc and Zr may considerably improve both strength and ductility of 7000 series aluminum alloys, which is associated with precipitation of fine coherent Al$_3$(Sc,Zr) particles. These particles also increase resistance to recrystallization and promote formation of a stable refined microstructure. Because of very low equilibrium solubility of Sc and Zr in Al alloys, a supersaturated solid solution of these elements in the Al matrix presented after casting is responsible for precipitation of the Al$_3$(Sc,Zr) particles during subsequent heat treatment, while the strengthening effect depends on the particle size and number density. Therefore, it is necessary to optimize precipitation of the Al$_3$(Sc,Zr) particles, in order to achieve superior balance of mechanical properties. In the present work, the effect of heat treatment conditions on microstructure and tensile properties of a developmental 7000 series Al alloy SSA018 modified with Sc and Zr was studied, with special emphasis on the analysis of size and number density of the Al$_3$(Sc,Zr) particles, and their effect on the strength increase. This work was published in *Materials Science Forum* by Senkov, Shagiev, and Miracle [29].

2.10.3 Effect of Sc on Aging Kinetics in a Direct Chill Cast Al-Zn-Mg-Cu Alloy

The effect of Sc additions on precipitation strengthening in a direct chill cast Al-Zn-Mg-Cu alloy was studied after natural and artificial aging. The microhardness, room temperature mechanical properties, and phase composition of the alloys were determined after different steps of aging. The strengthening mechanisms were discussed. It was shown that minor additions of Sc increased the strength of the Al-Zn-Mg-Cu alloy after casting and solution heat treatment, due to the precipitation of fine coherent Al$_3$(Sc,Zr) particles. An analysis of the aging kinetics revealed that Sc had no effect on the natural aging, which was controlled by the formation and growth of Guinier‑Preston (GP) I zones. On the other hand, the Sc additions accelerated the aging process at 120 °C and 150 °C within a period of time of the formation and growth of GP II zones and η′ particles. It was concluded that the presence of Sc accelerated the formation and growth of GP II zones in the Al-Zn-Mg-Cu alloys, which led to the earlier precipitation of the η′ phase. However, at longer aging times at 120 °C and 150 °C, the aging response of the Sc-containing alloys slowed down, due to faster coarsening of the η′ particles and their transformation into g particles. A model of the formation of vacancy-rich clusters, precursors to GP zones, in the Al-Zn-Mg‑based alloys was proposed. According to this model, the observed effects of Sc on aging are the result of the Sc-induced increase in the number density of the GP II clusters and the concentration of quenched-in solute-bound excess vacancies. This work was published in *Metallurgical and Materials Transactions A* by Senkov, Senkova, and Shagiev [30].

2.10.4 Particle Size Distributions during Diffusion Controlled Growth and Coarsening

Theoretical analysis of particle growth and coarsening conducted in the present work, which includes stochastic (random) flux of a solute inside/from the growing particles, predicts normal distribution of the particle sizes, independent of the particle volume fraction. This result agrees well with the numerous experimental data and it solves a long-time problem related with a non-symmetrical size distribution in earlier Lifshitz–Slyozov–Wagner theory. This work was published in *Scripta Materialia* by Senkov [31].

2.11 Published Research on Friction Stir Welding of Sc-Modified Al-Zn-Mg-Cu Extruded Plates

2.11.1 Friction Stir Welding of Sc-Modified Al-Zn-Mg-Cu Alloy Extrusions

Small additions of scandium to Al-Zn-Mg-Cu 7000 series alloys can significantly improve mechanical properties and augment the strength retention at low and elevated temperatures. This research program evaluates the residual properties of Sc-modified Al-Zn-Mg-Cu alloy extrusions joined through friction stir welding. Mechanical and corrosion testing were performed on the baseline material and on panels friction stir welded at 175, 225, 250, 300, 350 and 400 RPM (all other weld parameters held constant). A thermal model of friction stir welding is developed that utilizes an energy-based scaling factor to account for tool slip. The proposed slip factor is derived from an observed, empirical relationship between the ratio of the maximum welding temperature to the solidus temperature and energy per unit length of weld. The thermal model successfully predicts the maximum welding temperatures over a range of energy levels, and the mechanical and corrosion behavior is correlated to the temperature distribution predicted by the model. This work published in *2008 Proceedings of ASME International Mechanical Engineering Congress and Exposition, IMECE* by Hamilton, Sommers, and Senkov [32].

2.11.2 Friction Stir Welding of Sc-Modified Al-Zn-Mg-Cu Alloy Extrusions

Small additions of scandium to Al-Zn-Mg-Cu 7000 series alloys can significantly improve mechanical properties and augment the strength retention at low and elevated temperatures. This research program evaluates the residual properties of Sc-modified Al-Zn-Mg-Cu alloy extrusions joined through friction stir welding. Mechanical and corrosion testing were performed on the baseline material and on panels friction stir welded at 175, 225, 250, 300, 350 and 400 RPM (all other weld parameters were held constant). A thermal model of friction stir welding was developed utilizing an energy-based scaling factor to account for tool slip. The proposed slip factor is derived from an empirical relationship between the ratio of the maximum welding temperature to the solidus temperature and energy per unit length of weld. The thermal model successfully predicts the maximum welding temperatures over a range of energy levels, and the mechanical and corrosion behavior is correlated to the temperature distribution predicted by the model. This work was published in *Friction Stir Welding and Processing V, TMS* by Hamilton, Dymek, and Senkov [33].

2.11.3 Thermal Modeling of Friction Stir Welding of Sc-Modified Al-Zn-Mg-Cu Alloy

Small additions of scandium to Al-Zn-Mg-Cu 7000 series alloys can significantly improve mechanical properties and augment the strength retention at low and elevated temperatures. This

research program evaluates the residual properties of Sc-modified Al-Zn-Mg-Cu alloy extrusions joined through friction stir welding. Mechanical and corrosion testing were performed on the baseline material and on panels friction stir welded at 175, 225, 250, 300, 350 and 400 RPM (all other weld parameters were held constant). A thermal model of friction stir welding was developed utilizing an energy-based scaling factor to account for tool slip. The proposed slip factor is derived from an empirical relationship between the ratio of the maximum welding temperature to the solidus temperature and energy per unit length of weld. The thermal model successfully predicts the maximum welding temperatures over a range of energy levels, and the mechanical behavior is correlated to the temperature distribution predicted by the model. This work was published in *Computer Methods in Materials Science* by Hamilton, Dymek, and Senkov [34].

2.12   Published Research on CP-FEM Based Materials Modeling

2.12.1 A Combined Experimental and Simulation Study to Examine Lateral Constraint Effects on Microcompression of Single-Slip Oriented Single Crystals

A custom in-situ scanning electron microscope (SEM) mechanical testing system has been used to study the compressive deformation behavior of single-slip oriented Rene N5 microcrystals. Two different compression platens were used to explore the effect of lateral stiffness on the resultant mechanical response, which approximated either a high-friction or effectively zero-friction case. The change in the lateral constraint of the test system had a demonstrable effect on many aspects or attributes of plastic flow: the yield stress and strain-hardening behavior, the intermittency of strain bursts, the spatial distribution of slip bands, and the development of internal crystal rotations. Finite element modeling of the microcompression experiments using an anisotropic crystal plasticity framework provided insight regarding changes in the internal stress field and resultant activity of slip systems. The experimental findings are rationalized based on these simulation results. This work was published in *Acta Materialia* by Shade, Wheeler, Choi, Uchic, Dimiduk, and Fraser [35].

2.13   Published Research on Modeling of Dislocation Behaviors

2.13.1 Athermal Mechanisms of Size-Dependent Crystal Flow Gleaned from Three-Dimensional Discrete Dislocation Simulations

Recent experimental studies have revealed that micrometer-scale face-centered cubic (fcc) crystals show strong strengthening effects, even at high initial dislocation densities. We use large-scale three-dimensional discrete dislocation simulations to explicitly model the deformation behavior of fcc Ni microcrystals in the size range of $0.5\mu m$ to $20\ \mu m$. This study shows that two size-sensitive athermal hardening processes, beyond forest hardening, are sufficient to develop the dimensional scaling of the flow stress, stochastic stress variation, flow intermittency and high initial strain-hardening rates, similar to experimental observations for various materials. One mechanism, source-truncation hardening, is especially potent in micrometer-scale volumes. A second mechanism, termed exhaustion hardening, results from a breakdown of the mean-field conditions for forest hardening in small volumes, thus biasing the statistics of ordinary dislocation processes. This work was published in *Acta Materialia* by Rao, Dimiduk, Parthasarathy, Tang, Uchic, and Woodward [36].

2.13.2 Atomistic Simulations of Cross-Slip Nucleation at Screw Dislocation Intersections in Face-Centered Cubic Nickel

The Escaig model for thermally activated cross-slip in face-centered cubic (fcc) materials assumes that cross-slip preferentially occurs at obstacles that produce large stress gradients on the Shockley partials of the screw dislocations. However, it is unclear as to the source, identity and concentration of such obstacles in single-phase fcc materials. Embedded atom potential, molecular-statics simulations of screw character dislocation intersections with 120° forest dislocations in fcc Ni are described that illustrate a mechanism for cross-slip nucleation. The simulations show how such intersections readily produce cross-slip nuclei and thus may be preferential sites for cross-slip. The energies of the dislocation intersection cores are estimated and it is shown that a partially cross-slipped configuration for the intersection is the most stable. In addition, simple three-dimensional dislocation dynamics simulations accounting for Shockley partials are shown to qualitatively reproduce the atomistically determined core structures for the same dislocation intersections. This work was published in *Philosophical Magazine* by Rao, Dimiduk, El-Awady, Parthasarathy, Uchic, and Woodward [37].

2.13.3 Activated States for Cross-Slip at Screw Dislocation Intersections in Face-Centered Cubic Nickel and Copper via Atomistic Simulation

We extend our recent simulation studies where a screw dislocation in face-centered (fcc) Ni was found to spontaneously attain a low-energy partially cross-slipped configuration upon intersecting a forest dislocation. Using atomistic (molecular statics) simulations with embedded atom potentials, we evaluate the activation barrier for a dislocation to transform from fully residing on the glide plane to fully residing on a cross-slip plane intersecting a forest dislocation in both Ni and Cu. The activation energies were obtained by determining equilibrium configurations (energies) when variable pure tensile or compressive stresses are applied along the [111] direction on the partially cross-slipped state. We show that the activation energy is a factor of 2 to 5 lower than that for cross slip in isolation via the Escaig process. The cross-slip activation energies obtained at the intersection in Cu are in reasonable accord with the experimentally determined cross-slip activation energy for Cu. Further, the activation barrier for cross-slip at these intersections is shown to be linearly proportional to $(d/\mathbf{b})[\ln(1.732d/\mathbf{b})]^{1/2}$, as in the Escaig process, where d is the Shockley partial dislocation spacing and $\mathbf{b}$ is the Burgers vector of the screw dislocation. These results suggest that cross-slip should be preferentially observed at selected screw dislocation intersections in fcc materials. This work was published in *Acta Materialia* by Rao, Dimiduk, El-Awady, Parthasarathy, Uchic, and Woodward [38].

2.13.4 Trapping and Escape of Dislocations in Micro Crystals with External and Internal Barriers

We perform three-dimensional dislocation dynamics simulations of solid and annular pillars, having both free surface boundary conditions, or strong barriers at the outer and/or inner surfaces. Both pillar geometries are observed to exhibit a size effect where smaller pillars are stronger. The scaling observed is consistent with the weakest-link activation mechanism and depends on the solid pillar diameter, or the annular pillar effective diameter, $D_{eff} = D - D_i$, where D and D_i are the external and internal diameters of the pillar, respectively. An external strong barrier is observed to dramatically increase the dislocation density by an order of

magnitude due to trapping dislocations at the surface. In addition, a considerable increase in the flow strength, by up to 60 percent, is observed compared to simulations having free surface boundary conditions. As the applied load increases, weak spots form on the surface of the pillar by dislocations breaking through the surface when the RSS is greater than the barrier strength. The hardening rate is also observed to increase with increasing barrier strength. With cross-slip, we observe dislocations moving to other glide planes, and sometimes double-cross slipping, producing a thickening of the slip traces at the surface. Finally the results are in qualitative agreement with recent compression experimental results of coated and centrally filled micropillars. This work was published in *International Journal of Plasticity* by El-Awady, Rao, Woodward, Dimiduk and Uchic [39].

2.14   Published Research on Alloy Development

2.14.1 NbTiSiMo-X Alloys-Composition, Microstructure Refinement and Properties

Advanced NbTiSi-X alloys have demonstrated very high RT strength levels (compressive yield strength approaching 1,800 MPa) and excellent high-temperature strength retention (approximately 1,200 MPa at 1,000 ° C and over 500 MPa at 1,200 °C). Unfortunately, these alloys have an inhomogeneous size and spatial distribution of silicides, low fracture strength under tension (300 MPa) at all temperatures, and low oxidation resistance. The high volume fraction and non-uniform size distribution of silicides were considered to be responsible for the poor fracture resistance. In this work we attempt to refine the microstructure of cast alloys and to increase oxidation resistance by introducing Mo and adjusting other alloying additions. In focused efforts, we explored highly refined near-eutectic alloys, NbTiSiMo-Y, that showed excellent compression flow behavior. Further chemistry adjustments were made for balanced improvements, and cast alloys in homogenized material forms were evaluated for fracture to find that increases in fracture resistance without major chemistry modification are limited in the current alloy system. This work was published by *Storming Media* for conference paper preprint by Woodward, Kim, and Menon [40].

3   UNPUBLISHED RESEARCH

3.1   Unpublished Research on Advanced Metallics

3.1.1   CP-FEM Based Materials Modeling

3.1.1.1   Creep Constitutive Modeling of Ni-Base Single Crystal Superalloys [35]

The crystallographic constitutive model for creep of single crystal blade alloys was formulated. The model consists of slip-system based crystal plasticity and continuum damage mechanics. The former was formulated by accounting for micromechanisms responsible for creep behaviors at different temperatures and stresses. The micromechanisms incorporated are:

- Orowan resistance against <011> dislocation movement into narrow γ-matrix channels

- Formation of interfacial dislocation networks (IDNs) from <011> matrix dislocations; the IDN works as an effective barrier against <011> matrix dislocation glide.

- The stacking fault energy (SFE) of the γ matrix that controls the cross-slip behavior of <011> matrix dislocations, hence controlling the <011> dislocation density in the preferred matrix channels and the rate of IDN formation; the γ SFE effect reflects the Escaig effect.

- Formation of <112> SF pairs from reactions of <011> matrix dislocations

- Latent hardening of <112> SF slip due to interactions between <112> SF dislocations and between <112> SF dislocations and <011> matrix dislocations

- The influence of the γ-SFE on the γ' shearing behavior, hence the degree of orientation sensitivity

The continuum damage mechanics model is intended to cover micro-pore damage and all other damages that mainly contribute to secondary to tertiary creep behaviors.

Detailed parametric studies and adjustments were made, starting from prediction of orientation-sensitive primary & secondary creep in the low temperature, high stress regime. Primary results were presented in the research group meeting on Dec. 2008. It is generally believed that the orientation sensitivity of primary creep is due to γ'-precipitate shearing by <112> stacking fault (SF) dislocation ribbons. However, constitutive modeling in the LH regime indicated that even under <112> slip very dramatic softening and hardening terms are necessary to capture orientation-dependent primary creep in FEM simulations.

A plan for a limited number of creep and tensile tests, and the characterization was outlined. We contacted and received from Rolls Royce (Y-Q. Sun) eighteen CMSX-4 round bars and two flat bars (0.98"x4.72"x0.39"). All bars were cast along the [0 0 1]. The top and bottom of the bars were EDM cut and both ends are being electropolished for the Laue analysis. Upon completion of electropolishing the Laue analysis will be performed for each bar in order to determine the exact crystallographic orientation of each bar, and this information will be used to cut bars along

the crystallographic orientations for creep and tensile tests. We also contacted Rolls Royce to check the availability of additional CMSX-4 flat bars.

3.1.1.2 3D Microstructure Generation, Meshing and CP-FEM Approaches

3.1.1.2.1 3D Microstructure Generation and Meshing

The microstructure builder (MB), which is a series of codes for building synthetic 3D polycrystalline microstructures, was obtained from professor Rollett, Carnegie Mellon University. The original codes were Linux/Unix based and required different types of compilers. All codes were re-compiled and optimized under the Windows environment, and now the codes run smoothly under the batch mode at Windows. An effort was made to check the 'quality' of 3D grain geometries built by MB. The comparison of grain geometries between MB and experimental data from serial sectioning was found to be necessary. A 3D meshing tool was also found to be necessary to mesh the 3D grain geometries for the finite element plasticity simulation.

The codes for meshing a 3D polygrain geometry developed by Drs. Cornwell and Noack were obtained. The package consists of C/C++ codes, Python scripts and cmake that links these codes. All codes were compiled at a supercomputer at Ohio Supercomputer Center (OSC) since some of the codes were not complied in a Window PC due to a compatibility problem. The codes were finally optimized at an OSC machine after going through time-consuming debugging processes. An issue is that it takes 5 hours of CPU time (at OSC) to complete meshing of a simple 9-griain cubic box (with tetrahedrons). VTK (Visualization Tool-Kit) was chosen to visualize the output meshes, and making Python scripts is an ongoing subject in order to use VTK as a tool for visualizing the meshed polygrain.

The 3D polycrystalline microstructure obtained from serial sectioning of IN100 was meshed by engineers from Simmetrix (commercial meshing software) through Rollett of PET-HPCMP. The quality of 3D meshing was evaluated. The results showed a large fraction of high-aspect-ratio tetrahedral elements, which randomly distribute throughout the entire polycrystalline geometry. The boundary surface of the meshed 3D box was also uneven. The similar problem was already pointed out from the 3D polycrystalline geometry meshed using the Cornwell-Noack's code.

Three D meshing of 3D polycrystalline microstructures was attempted in collaboration with Professor Rollett of PETTT. The general meshing procedure for 3D polycrystalline microstructures obtained from serial sectioning is grain boundary smoothing, surface meshing of individual grains, and volume meshing of individual grains. Grain boundary smoothing and surface meshing codes were recently developed by Rollett's group. We utilized those codes in order to smooth and mesh grain boundaries of an IN100 microstructure taken from serial sectioning by M. Groeber. A box containing 429 grains was selected from the original IN100 microstructure, and grain boundary smoothing and meshing were performed using codes from Rollett's. The grain boundary smoothing result was acceptable even though the surface mesh quality still needs to be improved. The surface-meshed IN100 geometry was converted to the STL format and sent to Hugh Thornburg of AFRL/RCM to check the feasibility of volume meshing. Also, as a parallel effort open source volume meshing codes are being surveyed in

order to check the possibility of using those codes to mesh the volume of the surface-meshed IN100 microstructure.

3.1.1.2.2 CP-FEM Approaches for 3D Microstructures

A crystal plasticity (CP) FEM approach for real or synthetic 3D microstructures was roughly planned. The first step was going to be estimating the computational cost and resources for the CP-FEM simulation of the 3D microstructure. The talk entitled "FEM-Based Mechanical Modeling Approaches for Heterogeneous 3D Microstructures: Review" was presented at the workshop on "Microstructure Simulation and Mesh Generation for FE Analysis". The presentation was intended to develop basic ideas and methodologies for modeling mechanical responses for 3D realistic polycrystalline microstructures.

A series of FEM simulations were performed to evaluate the capability of HPC-MSRC computational resources for the ABAQUS static implicit analysis of a large-size polygrain geometry. The simulation box size was varied to 50^3, 70^3 and 80^3 8-noded brick elements, which contain 5^3, 7^3 and 8^3 cubic grains, respectively. The simple-tension boundary conditions were applied until the flow curve reaches the elasto-viscoplastic regime, which requires at least 70 time increments to achieve. It seems that the MSRC supercomputer can practically handle up to about 80^3 8-noded brick elements for the ABAQUS static implicit analysis. It requires about 1120 CPU hours to complete the analysis.

The parametric CP-FEM study was performed in order to clarify effects of the mesh type and stepped/smooth geometries on the distribution of elastic & plastic flow heterogeneities using a bicrystal sphere embedded in a cubic box. The first effort included the optimization of the ratio of the diameter (D) of the bicrystal sphere to the edge length (L) of the cubic box. An effort was made to generate smooth bicrystal spheres using tetrahedral and hexahedral elements, respectively. An open source meshing code (Gmsh) was used to mesh a bicrystal sphere using tetrahedral elements. The total number of tetrahedral elements was set such that the mesh density is equivalent between smooth tet-meshed and stepped cube-meshed bicrystal spheres. CP FEM simulations were performed to the tet-meshed bicrystal geometry and results were compared to those from the bicrystal sphere having a stepped geometry meshed by hexahedral elements. It was found that hex-meshed stepped grains and tet-meshed smooth grains exhibit the different statistical distribution (histogram) of a plasticity parameter. Depending on the choice of a plasticity parameter hex-meshed stepped grains and tet-meshed smooth grains show longer tail and head in histogram against each other. Those excess lower and upper plasticity values were located near grain boundaries. The comparison of spatial distribution of plasticity parameters indicated the inconsistent correspondence of local hot and cold spots between hex-meshed stepped and tet-meshed smooth grains. This implies that the stepped grain representation can alter the statistical distribution of plasticity and locality of hot and cold spots, particularly near the GB's. All these results were summarized in a talk entitled "A parametric crystal-plasticity FEM study for 3D polycrystalline Microstructures", which was presented in Plasticity 2010.

3.1.2 Modeling And Predictions of Materials Properties

3.1.2.1 Modeling On-Cooling Data on Waspalloy

In this reporting period, the previously calibrated model for Waspalloy was used to evaluate the effect of cooling rate on yield stress of waspalloy, using the data of Groh et al. The microstructural information given in the published article is reproduced below. Through a personal correspondence with the author, Rollie Dutton (AFRL/RX) obtained additional information as below.

Primary (Gr.Bdry) $\gamma' = 2\%$ Total Volume percent of $\gamma' = 32\%$

ASTM grain size 6-7 for all, 5-5.5 for oil quenched sample

Combining these, we obtained the following for the alloy microstructures, as shown in Table 1.

Table 1. Waspalloy Microstructural Parameters Studied

cooling rate	Grain Size	primary size	Primy Vf	secy size	secy vf	tery size	tery vf
9.9	38	2	0.02	0.4	0.105	0.16	0.195
45	38	2	0.02	0.35	0.105	0.12	0.195
72	38	2	0.02	0.3	0.156	0.07	0.144
113.4	38	2	0.02	0.3	0.246	0.06	0.054
261	38	2	0.02	0.3	0.246	0.06	0.054
315	58	2	0.02	0.3	0.3	0.04	0

Using this information for microstructures, the predicted yield strength was compared with reported yield strength at 1000 °F and 1400 °F. These are shown in Figure 1. Although the trends are found to be close, it is concluded that the model's accuracy of predictions is compromised by the possible chemical inhomogeneity in cast alloys, as is the case for Waspalloy.

Further upon analyzing the data of Groh (as shown in Figure 2), it was made clear that the yield strength at 1000F had a very weak dependence on cooling rate and secondary size; and a weak dependence on tertiary size. Figure 3shows the scatter in the data on Waspalloy collected from the three sources (Allvac, Groh and Rolls Royce) It is concluded that the model's accuracy of predictions is compromised by the possible chemical inhomogeneity in cast alloys, as is the case for Waspalloy.

(a)   (b)
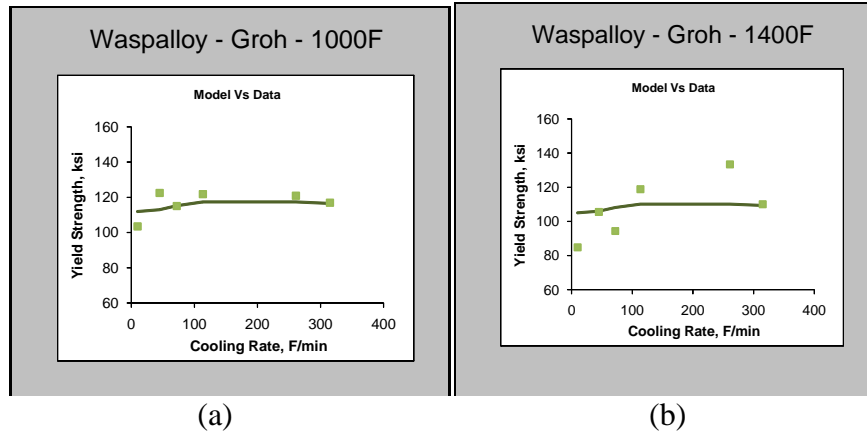
Figure 1. Predictions for Cooling Rate Effects (a) 1000 °F and (b) 1400 °F
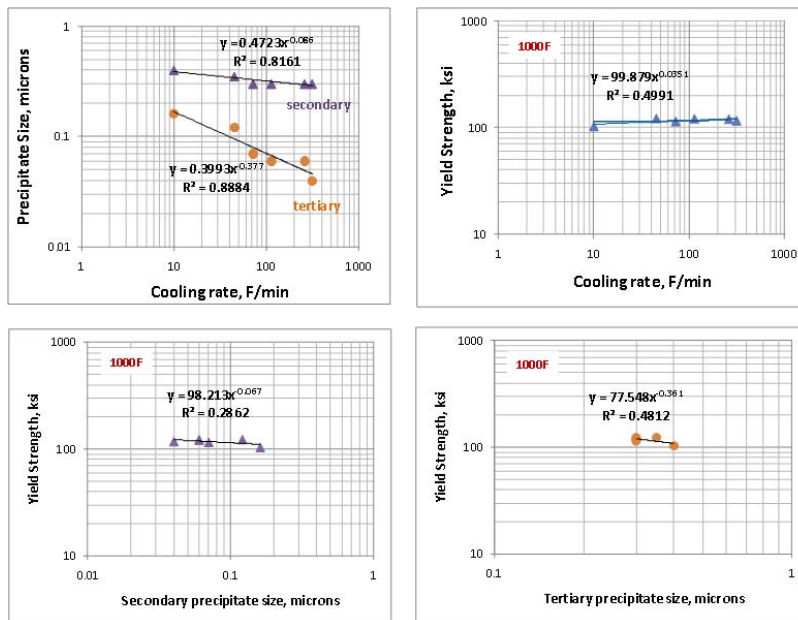
Figure 2. Analysis of Data: Very Weak Dependence on Precipitate Size
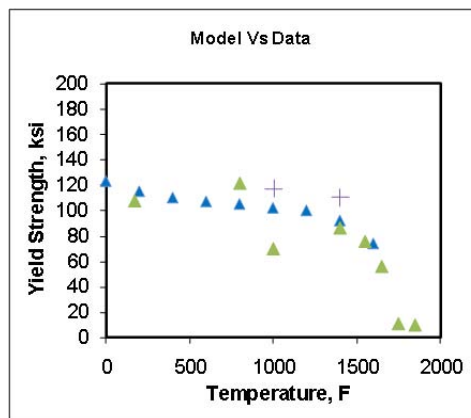


Figure 3. Significant Scatter in the Data

3.1.2.2 Modeling LSHR Microstructures using Precipicalc

In this reporting period, the software code Precipicalc was installed on a standalone laptop and the operating procedures learned. The software was used to evaluate the predictions of microstructures formed during subsolvus heat treatment of LSHR.

The composition of LSHR as given by NASA reports by Gabb et al., is given in Table 2.

Table 2. Composition of LSHAR in wt% (Gabb et al.) used in the Simulations

Al	B	C	Co	Cr	Fe	Mo	Nb	Ni (bal)
3.46	0.028	0.029	20.7	12.52	0.07	2.73	1.45	49.534

The results form PANDAT calculations using the composition in Table I gave the results for total volume fraction shown in Figure 4. Total Volume Fraction of γ′ in LSHR Predicted by LSH The solvus temperature was 2116 °F (1158 °C).
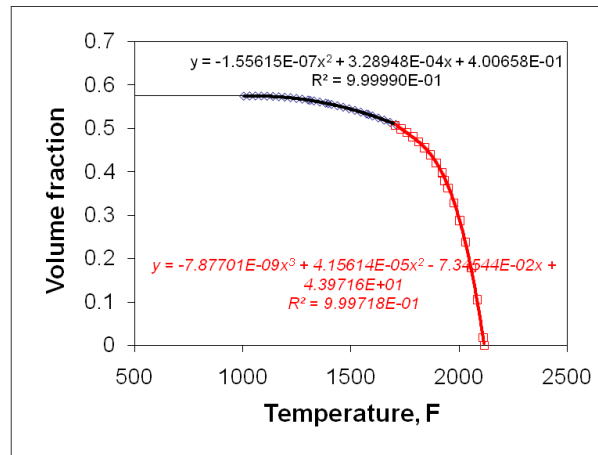
Figure 4. Total Volume Fraction of γ′ in LSHR Predicted by LSHR

Using the results from PANDAT, several runs of precipicalc were conducted that used subsolvus heat treatment as a starting point. All of these gave solutions that were contradictory to experimental data published by Gabb et al. A final run was made where an initial supersolvus heat treatment was included. The results are shown in Figure 5. The primary γ′ is seen to grow in preference to nucleation and growth of secondary and tertiary γ′, which is contrary to experimental data.

23
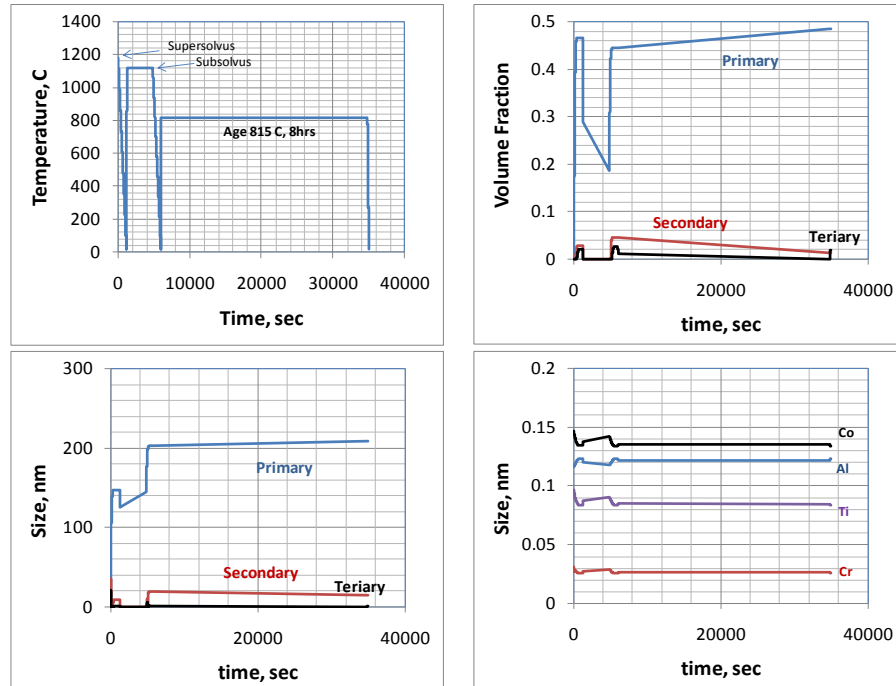
Figure 5. Heat Treatment Profile Predicted Microstructural Parameters and Chemistry

3.1.2.3   Modeling Multicple cracking in Alpha-Case

Several works have shown that titanium alloys develop an alpha-case when exposed to air at elevated temperatures for sufficient duration. It is also well known that the oxygen rich layer containing a high volume fraction of alpha, is brittle compared to the two-phase microstructure in the as processed condition. An interesting consequence of this has been reported on recently by John Porter and Reji John of AFRL/RXLMN. The surface layer was found to develop multiple cracks of fairly uniform periodicity upon tension testing.

A model was developed to rationalize the observations and to be able to predict alpha case thickness from crack spacing.

$$\lambda = \sigma_{c,crit} \, \frac{2h}{\tau}$$

$$\left(1-\nu^2\right)\left(\frac{\sigma_{c,crit}^2}{2\,E_c}\,h\,\frac{\lambda}{2} - \int_0^{\lambda/2}\frac{1}{E_c}\left(\frac{\tau}{h}\right)^2 h\,x^2\,dx\right) = \Gamma h$$

$$\sigma_{c,crit} = \left(\frac{6\,\Gamma\tau E_c}{h\left(1-\nu^2\right)}\right)^{1/3}$$

$$\lambda = 2\left(\frac{6\,\Gamma\,E_c}{\left(1-\nu^2\right)}\right)^{1/3}\left(\frac{h}{\tau}\right)^{2/3}$$

$$\frac{\sigma_\infty}{E_\infty} + \epsilon_{plastic} = \frac{\sigma_c}{E_c}$$

$$\tau = \frac{\sigma_{\infty,y}}{3\big/\sqrt{2}}$$

The model was found to predict the observed values for the Titanium 6242s measured by Porter and John, as well as Ti6-4 alloy reported on by Chan in *Mater. Trans*, 2008. In addition results on Cr films on polymer substrate were also found to be predicted well by the model. These are shown in Figure 6, Figure 7, and Figure 8.
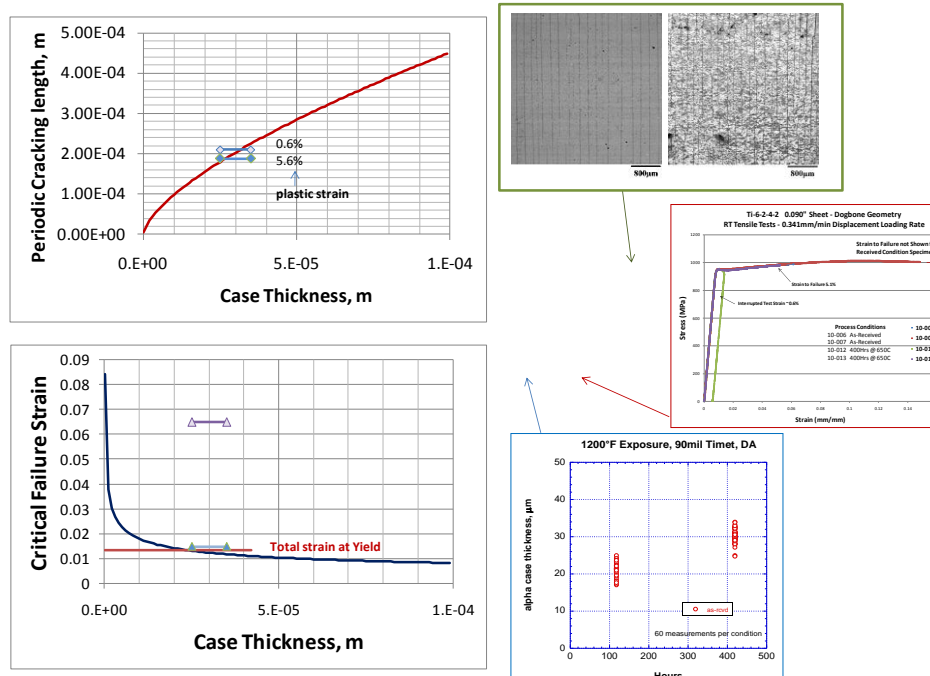
Figure 6. Model Predictions Compared with Data on Ti6242s by Porter and John
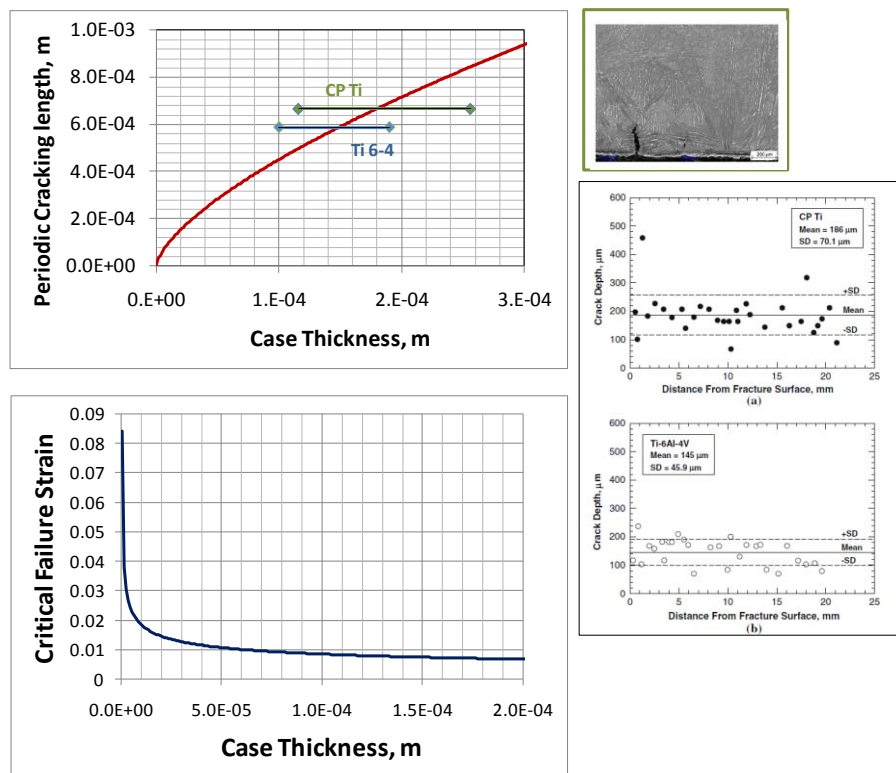
Figure 7. Model Predictions Compared with Data on Ti6-4 by Chan (2008)
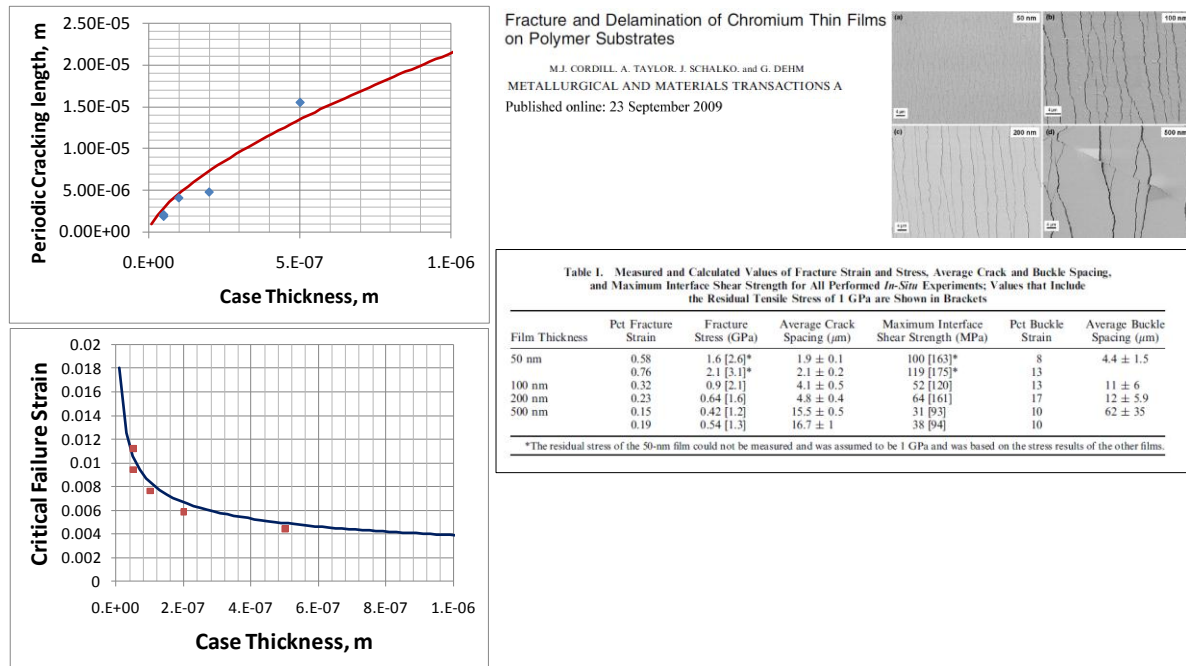
Figure 8. Model Predictions Compared with Data on Cr Films by Cordilla et al. (2009)

3.1.2.4 Alloy Development

3.1.2.5 Low Beta Containing Beta Gamma Alloys [20,41]

Significant effort was made in producing alloy 9CN and 9EN ISM ingots having the aim composition. The measured phase distribution and Al content in ISM ingots of the third batch alloys after a quasi-equilibrium heat treatment (900 °C/44h/AC), and the evaluation results listed in Table 3 indicate that the two ingots have improved chemistry and phase distribution with lowered beta phase volumes. Especially, the phase distribution in the 9EN ingot is very close to the desired values. In spite of lowered beta volumes, these alloys exhibit attractive microstructures in HIP'ed ingot materials, after hot extrusion as well as upon post-extrusion heat treatments. Some examples are shown Figure 9(a) for alloy 9CN. Figure 9 shows a Back-scattered Electron Image (BEI) image of the as-received ISM ingot in HIP'ed condition, which is featured by a fine-grained (~60µm) nearly fully lamellar microstructure with a phase distribution of $0.85g$-$0.11a_2$-$0.04B2$.

Table 3. Measured Phase Distribution and Al Content in ISM Ingots (900 °C/44h/AC)

Alloy (Nbeq)	Aim	Heat Treatment	γ (fr)	α2 (fr)	B2 (fr)	Ti-Al (at%)
9CN (10)	9C	900°C/44h /WQ	0.879	0.081	0.04	Ti-43.6Al
9EN 11.5)	9E	"	0.908	0.046	0.046	Ti-43.9Al
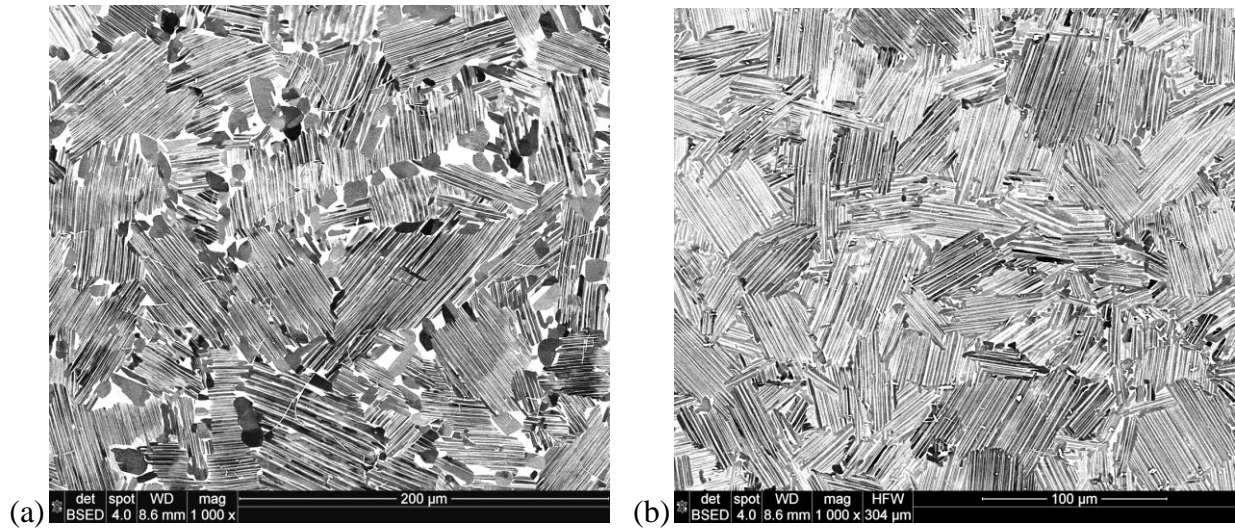
Figure 9. BEI Images of Alloy 9CN Ingot after (a) HIP'ing and (b) Hot Extrusion and Heat Treatments (1350 °C/30min/FC/900 °C/24h/AC)

A billet from each alloy ingot was hot extruded at 1240°C to a rectangular cross section rod form smoothly. Figure 9(b) shows a BEI image of the short transverse section of 9CN extrusion after a heat treatmtn (1350 °C/30min/FC/900 °C/20h/AC) that generated fully lamellar matrial with an attrractive lamellar feature and remakably fine (~60µm) grains. Ally 9EN showed similar phase and microstcuture features but with finer lkamellar spacing. Evaluation and mechanical property testing will be performed on these alloy materials in the follow-on IH project.

3.1.2.6 Nb-Si-Ti-X Alloy Development [41]

The study was aimed to develop $Nb(b)/Nb_5Si_3$ composite alloys that will have improved balance in mechanical properties and oxidation resistance. The strategy was to modify the chemistry of existing Nb-Ti-Si-X based alloys into a fine grained eutectic alloy system, Nb-Ti-Si-Y-Mo-Zr, where X and Y denote other alloying elements such as Al, Cr, Hf, Sn, etc. A series of alloy groups were produced in arc-melted cigar forms and given annealing treatments at 1500 °C. Alloys in Table 4 were evaluated for strengths under compression, fracture behavior under tension and cyclic oxidation resistance in the temperature range between RT and 1200 °C.

Table 4. Selected Alloy Compositions Measured by EPMA

Alloy-E	Nb	Ti	Si	Cr	Al	Hf	Zr	Mo
E69	50	12.5	16	5	3	3	3	7.5
DE1	46	12.5	18.5	5	1	2	5	10
LE1	40	12.5	18.5	5	1	3	10	10

The results are summarized below:

- Mo additions result in the refined microstructures in both as cast and annealed dendrite alloys and eutectic alloys. It is not practical with Nb-Ti-Si-Mo alloys having 16at% or greater Si.

- Remarkable intrinsic strength levels (yield strength ranging from 1600MPa to1850MPa) were achieved with Mo additions, indicating that Mo solid solution strengthens the beta phase; however, high high-temperature strength retention required sufficient Si content (>17 percent). Lowering the Ti content (from 18 percent to 12 percent, for example) enhances high temperature elongation.

- Premature brittle fracture takes place under tension (measured by bend test) at all temperatures, with fracture strength (FS) being less than 0.2YS at RT and close to YS at 1200 °C, Figure 10. The increase in fracture resistance with temperature, though gradual, has not been reported in any other systems. Nevertheless, the overall fracture strengths are too low for any rotational applications. Pronounced notch sensitivity at RT was observed with the fracture strength on notched bend bars ranging from 70MPa to 90MPa.

- Microstructure control to remove primary silicides is expected to enhance the fracture resistance. Judging from the present results, however, the improvements may still be inadequate for structural applications

- All Nb-(9-12.5)Ti-(16-19)Si-Y-(7.5-10)Mo-(3-10)Zr alloys show the highest oxidation rates at low temperatures around 800°C. In these fine-grained alloys, this can be explained by the cracking or separation of b/Nb5Si3 interfaces due to the oxidation-induced residual stresses produced in the beta phase, which then produces oxide spallation. The overall oxidation resistance therefore increases with temperature with the maximum occurring at 1000 °C with 10Mo+5Zr additions and around 1200 °C with 10Mo+10Zr additions.

- Based on the properties and oxidation behavior, alloy DE1 (Ti-46Al-12.5Ti-18.5Si-5Cr-1 duAl-2Hf-5Zr-10Mo) is recommended as the baseline alloy for future development effort (in terms of balance in strength-temperature relations and oxidation resistance).
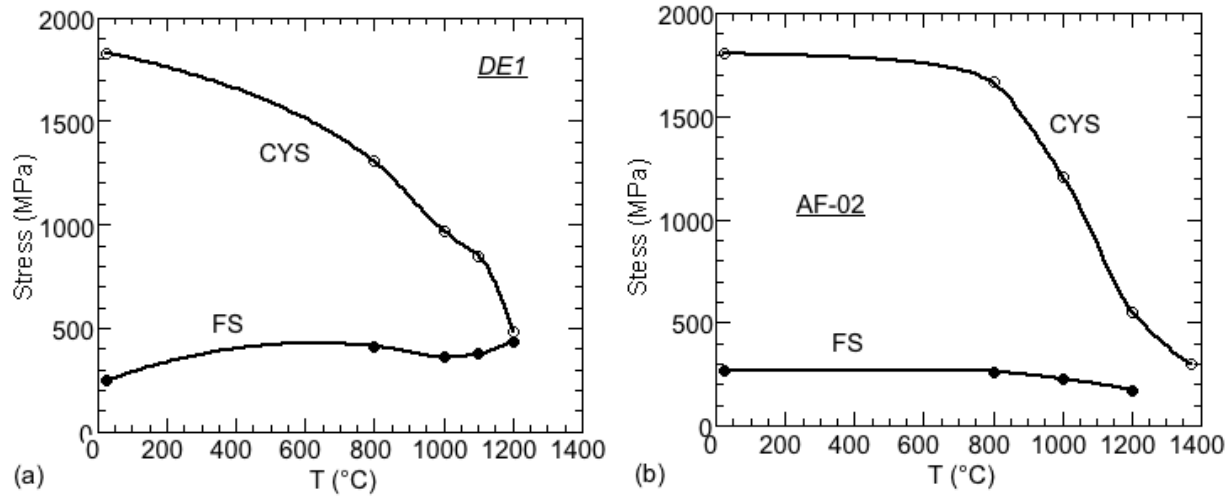
Figure 10. FS(tension) vs. Temperature and Yield Strength Measured (compression) for (a) Alloy DE1 and (b) Baseline Alloy AF02.

3.2 Unpublished Research on Functional Metals

3.2.1 Amorphous and Naocrystalline Metals

3.2.1.1 Mechanical Properties of Bulk Metallic Glasses

Uniaxial compression tests of $Mg_{54}Y_{11}Ag_7Cu_{28}$ bulk metallic glass were performed in the supercooled liquid region, at T = 468 K. and at a strain rate range of 5×10^{-4} to 2×10^{-3} s^{-1}. In the course of testing, shear thickening behavior was observed, where the magnitude of the peak stress increases with increasing initial strain rate. The deformation behavior of the glassy metal was discussed with emphasis on the commonly reported stress overshoot, strain softening behavior, and the previously unreported shear thickening behavior observed [22].

The deformation behavior was studied for a $Ca_{65}Mg_{15}Zn_{20}$ bulk metallic glass during monotonic compression, Vickers indentation hardness testing and compression–compression fatigue behavior. The alloy was macroscopically brittle, and demonstrated a dominant splitting failure with fracture planes from 0 to 20° relative to the loading axis. Secondary shear fracture was also observed in local regions, with a fracture plane roughly 35° relative to the loading direction. The nominal compressive fracture strength increased with an increase in the applied strain rate and was inversely proportional to the testing time. The indentation hardness decreased with an increase in the indentation load. The typical indentation morphology showed pile-ups near the indenter edges with associated shear bands. Although the fatigue data were somewhat scattered, a fatigue limit of 140 MPa was found at 10^6 cycles. Compared to Zr-based BMGs, the Ca65Mg15Zn20 BMG demonstrated much shorter fatigue lives and a lower fatigue endurance limit. Microstructural analysis showed that the $Ca_{65}Mg_{15}Zn_{20}$ amorphous alloy contains small spherical cavities. Under both monotonic and cyclic compression loadings of the samples, fractures initiated at these cavities and propagated in a direction generally parallel to the loading axis. Finite-element analysis (FEA) was used to model the fracture behavior. FEA of a centrally-located spherical void showed that under compression loading, large tensile stresses evolved in the cavities. The orientation of the maximum principal stress (P1) was found to be normal to the

direction of crack propagation, which is consistent with the experimental finding. Stresses in deeply-embedded adjacent voids and those in superficial voids were also studied. The influence of the void location in the cubical sample on the fracture behavior was quantitatively discussed [23,24].

3.2.1.2   Thermodynamic and Kinetic Behavior of Supercooled Glass-Forming Liquids

The temperature dependence of viscosity of glass-forming liquids near the glass transition temperature T_g (at which viscosity $\eta = 10^{12}$ Pa·s) is given by the fragility index $m = \dfrac{d \log_{10} \eta}{d\left(T_g / T\right)}\Bigg|_{T=T_g}$, which is unique for each material. Therefore, m should not depend on the type of the model functions used to describe the viscous behavior. Using this condition, the three-fitting-parameter viscosity equations, i.e. Vogel-Fulcher-Tammann (VFT) and Avramov equations, were modified into one-fitting parameter equations. Both modified equations contain the glass transition temperature T_g and fragility index m as material constants, allowing a direct comparison of the modified equations. Experimental viscosity data are required over a wide temperature range to determine the three fitting parameters of the VFT and Avramov equations, restricting their applicability. However, the modified equations developed here provide a convenient method of modeling the temperature dependence of viscosity by using the experimentally accessible parameters T_g and m. The modified one-fitting parameter equations were used to analyze viscous behavior of a number of oxide and organic glass-forming liquids. Based on this analysis, it was concluded that the modified Avramov equation describes the experimental data better than the modified VFT equation. Taking into account that the modified VFT equation predicts infinite viscosity at a finite temperature T_o, while the modified Avramov equation predicts a continuous increase in viscosity with a decrease in temperature down to the absolute zero, the obtained results may indicate that the oxide and organic supercooled liquids do not experience dynamic divergence when they are cooled below the glass transition temperature. Strong physical interpretations are developed for all of the parameters used in present equations to model the temperature dependence of viscosity, giving an important improvement over earlier phenomenological models [25].

Relaxation behavior of $Ca_{60}Mg_{20}Zn_{20}$, $Ca_{60}Mg_{20}Cu_{20}$, $Ca_{65}Mg_{15}Zn_{20}$, $Ca_{50}Mg_{20}Cu_{30}$, and $Ca_{55}Mg_{18}Zn_{11}Cu_{16}$ bulk metallic glasses and supercooled liquids was determined in the glass transition region using DSC with the heating rates from 1 to 160 K/min. The activation enthalpy of structural relaxation and the fragility index m were found to be smaller in the glassy state (onset of the glass transition) than in the supercooled liquid state (end of glass transition). The Ca-based glass-forming liquids showed strong behavior of the relaxation time, with the fragility indexes m in the range of 33 to 40. The strong liquid behavior implies sluggish kinetics of crystallization in the supercooled liquid region and explains the very good glass forming ability of these alloys. The critical cooling rate for amorphization R_c of the Ca-based bulk metallic glasses was estimated to be in the range of 0.3 to 10 K/s, which is similar to R_c values for the best Pd and Zr based metallic glass forming alloys discovered so far [26].

3.2.1.3 Super-High Strength Cast-and-Wrought Aluminum Alloys

3.2.1.4 Kinetics of Growth and Coarsening of Second Phase Particles

The effect of solution treatment on precipitation, growth and coarsening of coherent nanometer-sized $Al_3(Sc,Zr)$ particles and the effect of these particles on tensile properties of a direct chill (DC) cast Al-Zn-Mg-Cu-Sc-Zr alloy (SSA018) were studied. The size distribution, average size, number density and volume fraction of the $Al_3(Sc,Zr)$ particles were determined as a function of the solution treatment temperature and time. During solution treatment at temperatures 460 ^{o}C and 480°C, precipitation and growth of fine coherent $Al_3(Sc,Zr)$ particles from a super-saturated solid solution occurred. An increase in the solution treatment temperature resulted in $Al_3(Sc,Zr)$ particles with a larger mean diameter, higher volume fraction and lower number density. At both temperatures the precipitation reaction occurred rather slowly and even after holding for 48 hours at 460 ^{o}C the reaction only about ~ 65 percent complete, and at 480 ^{o}C the reaction was only about ~ 75 percent to 80 percent complete. The particle size distributions (PSDs) were symmetrical after all studied solution treatment conditions and were well described by a normal (Gaussian) distribution function. They did not follow the LSW theories of Ostwald ripening. The standard deviation, σ, and the mean particle size, d_m, of the PSDs were linearly dependent, so that an increase in d_m led to PSD broadening. The time dependence of the mean particle size was well described by both the diffusion-controlled and interface-reaction controlled processes. Analysis of the effect of heating rate on growth and analysis of the transformation kinetics with the use of the Kolmogorov-Johnson-Mehl-Avrami (KJMA) relationship led to selection of the reaction-limited process as the likely growth controlling process. It is also possible that the particle growth was controlled by a combination of both processes. The coherent nanometer-sized $Al_3(Sc,Zr)$ particles formed during solution treatment provided an additional Orowan strengthening of the SSA018 alloy, which increased with a decrease in the particle size and an increase in the particle volume fraction and varied from 75 MPa to 118 MPa after different heat treatments. After solution treatment and holding at room temperature for 24 hours, the Orowan strengthening from these particles provided from 40% to 63% of the yield strength increase relative to the alloy without the nanometer-sized $Al_3(Sc,Zr)$ particles. After aging at 120 °C for 19 hours, a substantial increase in both the yield strength and the ultimate strength was observed that was related to the precipitation of the *GP II* zones and *η′* phase particles while the $Al_3(Sc,Zr)$ particles provided ~ 18 percent to 28 percent of the yield strength increase of the alloy without these particles, which corresponded to ~ 15 percent to 22 percent of the total yield strength [28,29].

Theoretical analysis of particle growth and coarsening was conducted, which includes stochastic flux of a solute inside/from the growing particles. This analysis predicts normal distribution of the particle sizes, independent of the particle volume fraction. This result agrees well with the numerous experimental data and it solves a long-time problem related with a non-symmetrical size distribution in earlier Lifshitz-Slyozov-Wagner theory [31].

3.2.1.4.1 Friction Stir Welding of Sc-Modified Al-Zn-Mg-Cu Extruded Plates

Small additions of scandium to Al-Zn-Mg-Cu 7000 series alloys can significantly improve mechanical properties and augment the strength retention at low and elevated temperatures. This research program evaluates the residual properties of Sc-modified Al-Zn-Mg-Cu (SSA038) alloy

extrusions joined through friction stir welding (FSW). Mechanical and corrosion testing were performed on the baseline material and on panels friction stir welded at 175, 225, 250, 300, 350 and 400 RPM (all other weld parameters were held constant). Mechanical testing revealed the highest joint efficiency at 250 RPM, corresponding to an energy per unit length of weld of 1000 J/mm. The tensile strength falls off sharply when the welding energies surpass 1300 J/mm. The trend in mechanical properties may be due to the competition between secondary nucleation of strengthening phases that dominates at weld energies below 1300 J/mm and precipitate coarsening that dominates at energies above 1300 J/mm. A thermal model of friction stir welding was developed utilizing an energy-based scaling factor to account for tool slip. This model quantifies the welding temperatures above the aging temperatures of SSA038 and the dwell times above this temperature. The corrosion data are consistent with the trend in mechanical properties, i.e., the weld condition with the greatest susceptibility to corrosion corresponds to the weld condition that promotes the highest joint efficiency. For corrosion resistance, friction stir welding creates a performance gradient across the weld. The majority of exfoliation corrosion occurs along the thermo-mechanically affected zone boundary, but adjacent to the weld, the corrosion resistance in the significantly improves due to the overaging of the strengthening precipitates that occurs in this region. Away from the HAZ and into the parent material, the corrosion resistance returns to the baseline behavior. The individual regions around the weld were also rated in accordance with ASTM G34, the HAZ receiving an EA and the baseline/parent material receiving an EA/EB [32,33,34].

3.2.1.5 Materials for Thermal Management Applications

Several research groups around the globe have examined and developed the diamond containing metal matrix composites for more than the past decade. These composites also are commercially available in different chemistry-thermal property combinations. This HAZ class of materials is attractive for use as a substrate/ packaging material for electronic devices because of their relatively high thermal conductivity and a coefficient of thermal expansion (CTE), which can be tailored to match that of semiconductors. The matching of CTE is important to minimize the thermal stresses at the device/ package interfaces and thereby, to improve the component life/ reliability. In the current research, diamond-copper matrix composite was examined. The thermal conductivity was measured via laser flash techniques. To better understand the thermal transport coupling between constituents (i.e. Cu and diamond), the Cu/diamond interface was examined in more detail. A qualitative idea about the heat transport across the Cu/diamond interface was obtained via infra-red microscope observations. The best methodology to quantitatively measure the interface thermal conductance via time-domain thermoreflectance techniques was finalized. To aid in improved understanding of interfacial thermal transport, microstructural characterization of the interface region was also carried out. The characterization included high resolution transmission electron microcopy to examine the coherency and nanostructure of Cu, diamond and interface phase. The chemistry changes near the interface were evaluated via energy dispersive spectroscopy (EDS) and electron energy loss spectroscopy techniques in a transmission electron microscope (TEM) [42,43,44].

Thermal properties of a Cu-diamond composite with a silicon carbide interface layer were evaluated. A novel method, comprising two-step-coating of diamond particles followed by direct powder forging, for fabrication of this composite was employed. Interface structure and chemistry were examined via TEM techniques. The results indicate that the interface chemistry

has a strong influence on the thermal properties, such as thermal conductivity and coefficient of thermal expansion. In addition, to examine the effects of material variables on thermal properties, composites of different metal matrix chemistry and different diamond content were acquired. For the case of Cu-diamond composites, small amount (< 1 wt%) of boron or chromium was added in the Cu-matrix and diamond content was varied in the range 0 to 60 vol%. Moreover, silver-diamond composite was also acquired with an aim to evaluate its thermal properties and its interface structure/ chemistry.

3.3 Unpublished Research on Advanced TEM Techniques

3.3.1 Objective

The development of advanced TEM characterization techniques and methodologies to obtain microstructure parameters in the analysis of Ni base Superalloys in support of ISES.

An accurate description of the size and distribution nano-scale γ' precipitates is very crucial to the accelerated development of Ni-based superalloys. Due to the fine scale nature of these precipitates TEM was chosen to be the instrument of choice for the analysis. Consequently, a number of TEM imaging techniques including dark field imaging, high angle annular dark field imaging, EDS-X-Ray mapping and energy filtered transmission electron microscopy (EFTEM) were investigated to select the technique which best enabled rapid and extensive acquisition of these datasets using the engineering alloy, Rene 88DT. The EFTEM technique was found to be the most appropriate method for imaging fine γ' precipitates.

EFTEM Imaging techniques have been successfully developed using aberration corrected Titan 300 kV TEM for imaging the nano-scale γ' particles (5 nm to 300 nm). Imaging was attempted by deploying absorption edges from various elements contained in the model alloy, Rene 88DT such as Ni,Al,Ti,Cr and Co. Although imaging of the γ' precipitates was possible by using any of these elements, the best imaging conditions were obtained for Cr-L and Cr-M edges and especially exceptional for imaging tertiary γ' (<15 nm) particles.. This was due to larger differential partitioning of Cr between γ and γ'. Thus EFETEM imaging using Cr absorption edge will be the standard technique for imaging fine tertiary □' particles in various superalloys of interest to AFRL

High Resolution STEM Z-contrast imaging techniques were developed using aberration corrected Titan 300 kV TEM. Chemical partitioning effects were analyzed in Ni base superalloys and $SrTiO_2/BaTiO_2$ multilayers.

3.3.2 Research in Ni Base Superalloys

The skills learned from the development of EFTEM technique for fine nano-scale characterization of γ' precipitates were utilized in the investigation of coarsening of γ' studies in Ni- based superalloy Rene 88DT. Rene 88DT samples were solution treated and cooled at different cooling rates to ensure varying starting microstructure. These samples were then subjected to aging for varying lengths of time. TEM samples were prepared from these heat-treated materials. Both secondary and tertiary γ' precipitates were imaged in the TEM using the EFTEM technique developed earlier. From the TEM images precipitate sizes were measured by

image analysis. The experimental rate constants derived from this analysis were compared with analytical values deduced from two different models proposed in the literature, based on volume diffusion and bulk diffusion through the interface.

The skills learned from the High Resolution STEM Z-contrast imaging techniques were effectively utilized in analyzing the chemical partitioning effects in Ni base superalloys and $SrTiO_2/BaTiO_2$ multilayers. Detailed characterization of the γ/γ' interface was done using Z-contrast imaging technique to reveal the structural and compositional differences in the interface structure.

3.3.3 Other Projects

The following tasks were performed:

- Estimation of lattice parameter of γ' in constrained and unconstrained condition as a function of aging conditions via X-Ray (conventional and Synchrotron)

- Estimation of lattice parameter and volume fraction measurements in Ni-base superalloy Rene 88DT by Neutron Diffraction.

- Deformation Studies in Ti-6222 alloy

4 PUBLICATIONS and PRESENTATIONS

4.1 Publications

UES, Inc. employees or consultants working on the contract published the following papers:

1. "A Combined Experimental and Simulation Study to Examine Lateral Constraint Effects on Microcompression of Single-slip Oriented Single Crystals," P.A. Shade, R. Wheeler, Y.S. Choi, M.D. Uchic, D.M. Dimiduk, and H.F. Fraser, *Acta Materialia*, Vol. 57, p. 4580 (2009).

2. "A Method to Measure the Texture of Secondary Alpha in Bimodal Titanium-Alloy Microstructure," M.G . Glavicic, J.D. Miller, and S.L. Semiatin, *Scripta Materialia*, Vol. 54, p. 281 (2006).

3. "A Ternary Phase-Field Model Incorporating Commercial CALPHAD Software," Y.H. Wen, J.V. Lill, S.L. Chen, and J.P. Simmons, *Acta Materialia*, Vol. 58, p. 875 (2010).

4. "Activated States for Cross-Slip at Screw Dislocation Intersections in Face-Centered Cubic Nickel and Copper via Atomistic Simulation," S. Rao, D.M. Dimiduk, J.A. El-Awady, T.A. Parthasarathy, M.D. Uchic, and C. Woodward, *Acta Materialia*, in press (2010).

5. "Athermal Mechanisms of Size-Dependent Crystal Flow Gleaned from Three-dimensional Discrete Dislocation Simulations," S. Rao, D.MJ. Dimiduk, T.A. Parthasarathy, M. Tang, M.D. Uchic, and C. Woodward, *Acta Materialia*, Vol. 56, p. 3245 (2008).

6. "Atomistic Simulations of Cross-Slip Nucleation at Screw Dislocation Intersections in Face-Centered Cubic Nickel," S.I. Rao, D.M. Dimiduk, J.A. El-Awady, T.A. Parthasarathy, M.D. Uchic, and C. Woodward, *Philosophical Magazine*, Vol. 89, p. 3351 (2009).

7. "Cavitation during Hot-Torsion Testing of Ti-6Al-4V," P.D. Nicolaou, J.D. Miller, and S.L. Semiatin, *Metallurgical and Materials Transactions A*, Vol. 36A, p. 3461 (2005).

8. "Constitutive Modeling of Low-Temperature Superplastic Flow of Ultrafine Ti-6Al-4V Sheet Material," S.L. Semiatin and G.A. Sargent, *Key Engineering Materials Journal*, by *Trans Tech Publications*, Switzerland, Vol. 433, p.235 (2010).

9. "Defect Occurrence and Modeling for the Thermomechanical processing of Aerospace Alloys," S.L. Semiatin, P.D. Nicolaou, J.P. Thomas, and T.J. Turner, *Journal of Engineering Materials and Technology*, Vol. 130, Issue 2, p. 1001 (2008).

10. "Deformation and Recrystallization during Thermomechanical Processing of a Nickel-Base Superalloy Ingot Material," S.L. Semiatin, D.S. Weaver, R.L. Goetz, JU.P. Thomas, and T.J. Turner, *Materials Science Forum*, Vol. 550, p. 129 (2007).

11. "Description of the Fragile Behavior of Glass Forming Liquids with the Use of Experimentally Accessible Parameters," Oleg N. Senkov and Daniel B. Miracle, *Journal of Non-Crystalline Solids*, 355, p.2596 (2009).

12. "Dynamic-Coarsening Behavior of an α/β Titanium Alloy," S.L. Semiatin, M.W. Corbett, P.N. Fagin, G.A. Salishchev, and C.S. Lee, *Metallurgical and Materials Transactions A*, Vol. 37A, p. 1125, (2006).

13. "Effect of Deformation and Prestrain Mode on the Flow Behavior of Ti-6Al-4V," P.D. Nicolaou and Sheldon L. Semiatin, submitted for publication in *Materials Science Engineering A*.

14. "Effect of Strain-Path Reversal on Microstructure Evolution and Cavitation during Hot Torsion Testing of Ti-6Al-4V," P.D. Nicolaou and S.L. Semiatin, *Metallurgical and Materials Transactions A*, Vol. 38A, p. 3023 (2007).

15. "Effect of Stress and Strain Path on Cavity Closure during Hot Working of an Alpha/Beta Titanium Alloy," P.D. Nicolaou, R.L. Goetz, and S.L. Semiatin, *Metallurgical and Materials Transactions A*, Vol. 39A, p. 659, (2008).

16. "Local Interface Effects on Coalescence Kinetics in Ni-base Alloys," Y.H. Wen, J.P. Simmons, and C. Woodward, *Modelling Simulation in Materials Science and Engineering*, Vol. 18, No. 5, 055002, 9 pages (2010).

17. "Low-Temperature Coarsening and Plastic Flow Behavior of an Alpha/Beta Titanium Billet Material with an Ultrafine Microstructure," G.A. Sargent, A.P. Zane, P.N. Fagin, A.K. Ghosh, and S.L. Semiatin, *Metallurgical and Materials Transactions A*, Vol. 39A, p. 2949 (2008).

18. "Microstructural Changes and Estimated Strengthening Contributions in a Gamma Alloy Ti-45Al-5NB Pack-Rolled Sheet," Y-W. Kim, A. Rosenberger, and D.M. Dimiduk, *Intermetallics*, Vol. 17, Issue 12, p.1017 (2009).

19. "Modeling and Simulation of Texture Evolution during the Thermomechanical Processing of Titanium Alloys," S.L. Semiatin, M.G. Glavicic, S.V. Shevchenko, and O.M. Ivasishin, *ASM Handbook 22A: Fundamentals of Modeling for Metal Processing*, Edited by David Furrer and S.L. Semiatin (2010).

20. "Modeling of Texture Evolution during Hot Forging of Alpha/Beta Titanium Alloys," M.G. Glavicic, R.L. Goetz, D.R. Barker, G. Shen, D. Furrer, A. Woodfield, and S.L. Semiatin, *Metallurgical and Materials Transactions A*, Vol. 39A, p. 887, (2008).

21. "NbTiSiMo-X Alloys – Composition, Microstructure Refinement and Properties," TMS Proceedings TMS 2009, San Francisco, CA (2009).

22. "Overview of Experiments on Microcrystal Plasticity in FCC-derivative Materials: Selected Challenges for Modeling and Simulation of Plasticity," *Modeling and Simulations in Materials Science Engineering*, Vol. 15, p. 135 (2007)

23. "Plastic Flow and Microstructure Evolution during Low-Temperature Superplasticity of Ultrafine Ti-6Al-4V Sheet Material," S.L. Semiatin, P.N. Fagin, J.F. Betten, A.P. Zane, A.K.

Ghosh, and G.A. Sargent, *Metallurgical and Materials Transactions A*, Vol. 41A, p. 499 (2009).

24. "Relaxation Behavior of Ca-based Bulk Metallic Glasses," Oleg N. Senkov and Daniel B. Miracle, *Metallurgical and Materials Transactions A*, Online 3 Sep 2009.

25. "Systematic Approach to Microstructure Design of Ni-Base Alloys Using Classical Nucleation and Growth Relations Coupled with Phase Field Modeling," Billie Wang, Y.H. Wen, Jeff Simmons, and Yunzhi Wang, *Metallurgical and Materials Transactions A*, Vol. 39A, p.984 (2008).

26. "The Effect of Strain-Path Reversal on Cavitation during Hot Torsion of Ti-6Al-4V" P.D. Nicolaou and S.L. Semiatin, Metallurgical and Materials Transactions A, Vol. 37A, p. 3697 (2006).

27. "The Origins of Microtexture in Duplex Ti Alloys," M.G. Glavicic, B.B. Bartha, S.K. Jha, and C.J. Szczepanski, *Materials Science and Engineering A*, Vol. A513, p. 325 (2009).

28. Trapping and Escape of Dislocations in Micro Crystals with External and Internal Barriers," J.A. El-Awady, S.I. Rao, C. Woodward, D.M. Dimiduk, and M.D. Uchic, *International Journal of Plasticity*, 30 June 2010.

29. "X-ray Line-Broadening Investigation of Deformation during Hot Rolling of Ti-6Al-4V with a Colony-Alpha Microstructure," M.G. Glavicic and S.L., *Acta Materialia*, Vol. 54, p. 5337 (2006).

4.2   Presentations

UES, Inc. employees or consultants working on the contract made the following presentations:

1. "Coarsening and Plastic Flow of Ti-6Al-4V with an Ultrafine Microstructure," by G.A. Sargent, D. Li, and S.L. Semiatin, Presented by G.A. Sargent, AeroMat 2006, Seattle, WA, May 2006.

2. "Texture Modeling of Industrial Forging Practices in Ti-6Al-4V" by M.G. Glavicic, D.R. Barker, R.L. Goetz, and S.L. Semiatin, Presented by M.G. Glavicic, AeroMat 2006, Seattle, WA, May 2006.

3. "Integration of a Texture-Modeling Package into DEFORM™," by M.G. Glavicic, R.L. Goetz, D.R. Barker, D. Boyce, P.R. Dawson, and S.L. Semiatin, Presented by M.G. Glavicic, AeroMat 2007, Baltimore, MD, June 2007.

4. "Low-Temperature Coarsening and Plastic Flow of Ti-6Al-4V with an Ultrafine Microstructure," G.A. Sargent, D. Li, and S.L. Semiatin, Presented by G.A. Sargent, AeroMat 2007, Baltimore, MD, June 2007.

5. "The Variant Selection Process in an Alpha/Beta Titanium Alloy" by M.G. Glavicic, J.R. Calcaterra, D.U. Furrer, and S.L. Semiatin, Presented by M.G. Glavicic,. AeroMat 2007, Baltimore, MD, June 2007.

6. "An In-Situ Investigation of Strain Partitioning and Variant Selection Process in Ti-6Al-4V at Elevated Temperatures Using Synchrotron Radiation," by M.G. Glavicic, G. Sargent, N. Frey, P. Fagin, M. Scott, J. Almer, and S.L. Semiatin, Presented by M.G. Glavicic, TSM 2008, New Orleans, LA, March 2008.

7. "Low-Temperature Coarsening and Superplastic Flow of Ultrafine Ti-6Al-4V," by S.L. Semiatin and G.A. Sargent, Presented by G.A. Sargent, TMS 2008, New Orleans, LA, March 2008.

8. "Low-Temperature Superplastic Flow of Ultrafine Ti-6Al-4V," by G.A. Sargent, D. Li, and S.L. Semiatin, AeroMat 2008, Austin, TX, June 2008.

9. "Modeling of Phase Transformations in Ti Alloys," by A. Chatterjee, D. Furrer, M.G. Glavicic, S.L. Semiatin, and J. Miller, Presented by M.G. Glavicic, AeroMat 2008, Austin, TX, June 2008.

10. "Stochastic Flow and Size Effects in Microcrystal Plasticity," by D.M. Dimiduk, C. Woodward, S.I. Rao, M.D. Uchic, E. Nadgorny, and R. LeSar, Presented by S.I. Rao, MRS Fall Meeting, Boston, MA, December 2008.

11. "A New Microstructure-Sensitive Crystallographic Constitutive Models for Creep of Ni-base Single-Crystal Blade Alloys," by Y.S. Choi, Y-H. Wen, T.A. Parthasarathy, C. Woodward, D.M. Dimiduk, and M.D. Uchic, Presented by Y.S. Choi, TMS 2009, San Francisco, CA, February 2009.

12. "Beta Gamma Alloys Development of Robust Gamma TiAl Based Alloys," by Y-W. Kim, S-L. Kim, D.M. Dimiduk, and C. Woodward, Presented by Y-W. Kim, TMS 2009, San Francisco, CA, February 2009.

13. "NbTiSi-X – Composition-Processing-Microstructure-Properties" by Y-W. Kim, S. Menon, C. Woodward, Presented by Y-W. Kim, TMS 2009, San Francisco, CA, February 2009.

14. "Relaxation Behavior of Ca-based Bulk Metallic Glasses," by Oleg N. Senkov and Daniel B. Miracle, Presented by Oleg N. Senkov, TMS 2009, San Francisco, CA February 2009.

15. "Thermal Transport in Diamond Containing Metal Matrix Composites," by V. Sinha, S. Ganguli, R. Wheeler, J.L. Remmert, and J.E. Spowart, Presented by Vikas Sinha at the Symposium T: Nanoscale Heat Transport – From Fundamentals to Devices, MRS Spring Meeting, San Francisco, CA, April 2009.

16. "Plastic Flow and Microstructure Evolution During Low Temperature Superplasticity of Ultrafine Ti-6Al-4V Sheet Material," by S.L. Semiatin and G.A. Sargent, Presented by G.A. Sargent, AeroMat 2009, Dayton, OH, June 2009.

17. "Plastic Flow and Microstructure Evolution During Low Temperature Superplasticity of Ultrafine Ti-6Al-4V Sheet Material," by G.A. Sargent and S.L. Semiatin, Presented by G.A. Sargent, International Conference on Superplasticity in Advanced Materials (ICSAM) 2009, Seattle, WA, June 2009.

18. "A Review of Crystal-Plasticity FEM Studies for Polycrystalline Microstructures," by Yoon Suk Choi, Dennis M. Dimiduk, Christopher Woodward, Michael D. Uchic, Michael A. Groeber, Triplicane A. Parthasarathy, Presented by Yoon Suk Choi, USNCCM-10, Columbus, OH, July 2009.

19. "Beta Gamma Alloys Development of Robust Gamma TiAl Based Alloys," by Y-W. Kim, S-L. Kim, D.M. Dimiduk, and C. Woodward, Presented by Y-W. Kim, GKSS Thermec Conference, Berlin, Germany, August 2009.

20. "Thermal Transport in Diamond Containing Metal Matrix Composites," by V. Sinha, S. Ganguli, R. Wheeler, J.L. Remmert, and J.E. Spowart, Presented by Vikas Sinha, at the Symposium E13: Materials for Thermal Management (Heat Sink Materials), European Congress on Advanced Materials and Processed (EUROMAT) 2009, Glasgow, UK, September 2009.

21. "Atomistic Simulations of Cross-Slip Nucleation at Screw Dislocation Intersections in Face-Cubic Nickel" by S.I. Rao, D.M. Dimiduk, J.A. El-Awady, T.A. Parthasarathy, M.D. Uchic, and C. Woodward, Presented by S.I. Rao at TMS Annual Meeting, Seattle, WA, February 2010.

22. "Role of Silicon Carbide Interface Layer on Thermal Properties of a Copper-Diamond Composite," by V. Sinha, S. Ganguli, R. Wheeler, J.L. Remmert, and J.E. Spowart, Presented by Vikas Sinha, TMS Annual Meeting, Seattle, WA, February 2010.

4.3 Selected, Limited Distribution Reports

1. "MAI Ti Modeling 2, " as submitted to AFRL/RXLMP, June 2010, by Michael G. Glavicic, Robert L. Goetz, Douglas R. Barker, Gangshu Shen, David Furrer, Amit Chatterjee, Andrew Woodfield, and S.L. Semiatin, November 2007.

REFERENCES

1. Glavicic, M.G., Miller, J.D. and Semiatin, S.L., *Scripta Mater.*, 2006, 54, 281.

2. Glavicic, Goetz, R.L. Barker, D.R., Shen, G., Furrer, D., Woodfield, A., and Semiatin, S.L. *Metall. and Mater. Trans.*, 2008, 39A, 887.

3. Semiatin, S.L., Glavicic, M.G., Shevchenko, S.V., and Ivasishin, O.M., ASM Handbook, 22A, 2010.

4. Glavicic, M.G., Bartha, B.B, Jha, and Szczepanski, C.J., *Mater. Sci. Eng.*, 2009, A513, 325.

5. Glavicic, M.G. and Semiatin, S.L., *Acta Mater.*, 2006, 54, 5337.

6. Nicolaou, P.D., Miller, J.D., and Semiatin, S.L. *Metall. and Mater. Trans.*, 2005, 36A, 3461.

7. Nicolaou, P.D. and Semiatin, S.L. *Metall. and Mater. Trans.*, 2006, 37A, 3697.

8. Nicolaou, P.D. and Semiatin, S.L., *Metall. and Mater. Trans.*, 2007, 38A, 3023.

9. Nicolaou, P.D., Goetz, R.L., and Semiatin, S.L., *Metall. and Mater. Trans.*, 2008, 39A, 659.

10. Nicolaou, P.D. and Semiatin, S.L., submitted for publication in *Mater. Sci. Eng.*

11. Semiatin, S.L., Corbett, M.W, Fagin, P.N., Salishchev, G.A., and Lee, C.S., *Metall. and Mater. Trans.*, 2006, 37A, 1125.

12. Sargent, G.A., Zane, A.P., Fagin, P.N., Ghosh, A.K., and Semiatin, S.L., *Metall. and Mater. Trans.*, 2008, 39A, 2949.

13. Semiatin, S.L., Fagin, P.N., Betten, J.F., Zane, A.P., Ghosh, A.K., and Sargent, G.A., *Metall. and Mater. Trans.*, 2010, 41A, 499.

14. Semiatin, S.L. and Sargent, G.A., *Key Eng. Mater. J. by Trans Tech Pub.*, 2010, 433, 235.

15. Semiatin, S.L., Weaver, D.S., Goetz, R.L., Thomas, J.P., and Turner, T.J., *Mater. Sci. Forum*, 2007, 550, 129.

16. Semiatin, S.L., Nicolaou, P.D., Thomas, J.P., and Turner, T.J., *J. Eng. Mater. and Tech.*, 2008, 130, 2, 021001.

17. Wen, Y.H., Lill, J.V., Chen, S.L., and Simmons, J.P., *Acta Mater.*, 2010, 58, 875.

18. Wen, Y.H., Simmons, J.P., and Woodward, C., *Modelling Simul. Mater. Sci. Eng.*, 2010, 18, 055002.

19. Wang, Billie, Wen, Y.H., Simmons, Jeff, and Wang, Yunzhi, *Metall. and Mater. Trans.*, 2008, 39A, 984.

20. Kim, Y-W, Rosenberger, A., and Dimiduk, D.M., *Intermetallics,* 2009, 17, 1017.

21. Kim, Young-Won, to be submitted for publication as a AFRL-RX Technical Report, 2010.

22. Ross, Neal C., Mishra, Rajiv S., Senkov, Oleg N., and Miracle, Daniel B., *Metall. Mater. Trans. A*, 2009, 50, 1.

23. Wang, G., Liaw, P.K., Senkov, O.N., Miracle, D.B., and Morrison, M.L., *Adv. Eng. Materials*, 2009, 11, 1-2, 27.

24. Raphael, J., Wang, G.Y., Liaw, P.K., Senkov, O.N., and Miracle, D.B., *Metall. Mater. Trans. A*, DOI: 10.1007/s11661-009-0024-x.

25. Senkov, Oleg N. and Miracle, Daniel B., *J. of Non-Cryst. Solids*, 2009, 355, 2596.

26. Senkov, O.N., Miracle, D.B., *Metall. Mater. Trans. A*, 2009, DOI: 10.1007/s11661-009-9981-3.

27. Senkov, O.N., *Materials Sci. Forum*, 2009, 604-605, 155.

28. Senkov, O.N., Shagiev, M.R., Senkova, S.V., Miracle, D.B., *Acta Mater.,* 2008, 56, 3723.

29. Senkov, O.N., Shagiev, and Miracle, D.B., *Materials Sci. Forum*, 2009, 604-605, 113.

30. Senkov, O, Senkova, S.V., and Shagiev, M.R., *Metall. Mater. Trans. A*., 2008, 39, 1034.

31. Senkov, O.N., *Scripta Mater.*, 2008, 59, 171.

32. Hamilton, C., Sommers, A., and Senkov, O.N., *2008 Proceedings of ASME International Mechanical Engineering Congress and Exposition, IMECE 2008,* 2009, 4, 257.

33. Hamilton, C., Dymek S., and Senkov, O., *Friction Stir Welding and Processing V*, 2009, 315.

34. Hamilton, C., Dymek, S., and Senkov, O, *Computer Methods in Mater. Sci*, 2009, 9, 416.

35. Shade, P.A., Wheeler, R., Choi, Y.S., Uchic, M.D., Dimiduk, D.M., and Fraser, H.L., *Acta Mater.*, 2009, 57, 4580.

36. Rao, S., Dimiduk, D.M., Parthasarathy, T.A., Tang, M., Uchic, M.D., and Woodward, C., *Acta Mater.*, 2008, 56, 3245.

37. Rao, S.I., Dimiduk, D.M., El-Awady, J.A., Parthasarathy, T.A., Uchic, M.D., and Uchic, M.D., *Phil. Mag.*, 89, 2009, 3351.

38. Rao, S., Dimiduk, D.M., El-Awady, J.A., Parthasarathy, T.A., Uchic, M.D., and Woodward, C., *Acta Mater*., 2010, in press.

39. El-Awady, J.A., Rao, S.I., Woodward, C., Dimiduk, D.M., and Uchic, M.D., *Int. J. of Plasticity*, 30 Jun 2010.

40. Woodward, C., Kim, Y-W., and Menon, S., *Storming Media*, Conference Paper Preprint (2009).

41. Kim, Y-W, Kim, S-L, Dimiduk, D., and Woodward, C., In preparation for publication (2010).

42. Sinha, V., Ganguli, S., Wheeler, R., Remmert, J.L., and Spowart, J.E., MRS Spring Meeting (2009).

43. Sinha, V., Ganguli, S., Wheeler, R., Remmert, J.L., and Spowart, J.E., EUROMAT (2009).

44. Sinha, V., Ganguli, S., Wheeler, R., Remmert, J.L., and Spowart, J.E., TMS Annual Meeting (2010).

LIST OF ACRONYMS

AFRL   Air Force Research Laboratory
ALA   As large as
BEI   Back-scattered Electron Image
BMG   Bulk metallic glass
CP   Crystal plasticity
CTE   Coefficient of thermal expansion
DSC   Differential scanning calorimetry
EBSD   Electron backscatter diffraction
ECAE   Equal channel angular extrusion
EDS   Energy dispersive spectroscopy
EFTEM   Energy filtered transmission electron microscopy
Fcc   face-centered cubic
FEM   Finite element method
FS   Fraction strength
FSW   Friction stir welding
GBS   Grain-boundary sliding
GND   Geometrically necessary dislocations
GP   Guinier-Preston
HAZ   Heat affected zone
IDN   Interfacial dislocation networks
LApp   Los Alamos polycrystalline plasticity
MB   Microstructure builder
MPL   Materials Processing Laboratory
OIM   Orientation imaging microscopy
OSC   Ohio Supercomputer Center
PSD   Particle size distribution
SFE   Stacking fault energy
SEM   Scanning electron microscope
SP   Superplastic
TEM   Transmission electron microscope
TPS   Thermal Protection System
VFT   Vogel-Fulcher-Tammann
VTK   Visualization Tool-Kit